Infrasound Observations for Source and Path Effects

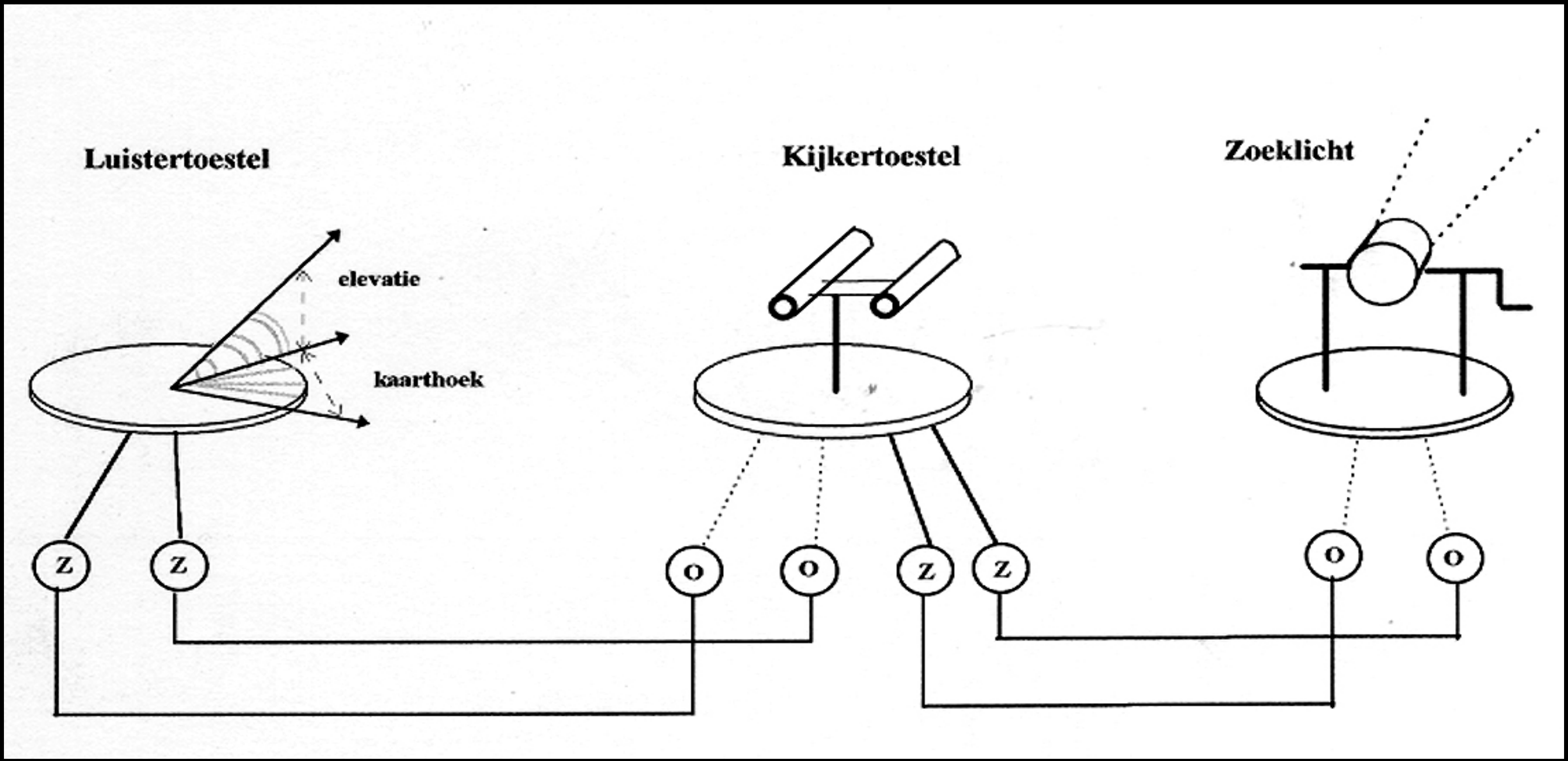

Junghyun Park, Chris Hayward, and Paul Golden Southern Methodist University

Il-Yeong Che and Jeong-Soo Jeon, Korea Institute of Geoscience and Mineral Resources

Mihan McKenna (ERDC), Stephen Arrowsmith (SNL), Phil Blom (LANL), Omar Marcillo (LANL), Michael Pasyanos (LLNL), Keehoon Kim (LLNL), Doug Drob (NRL)

Historic images provided by Laslö Evers

Motivation

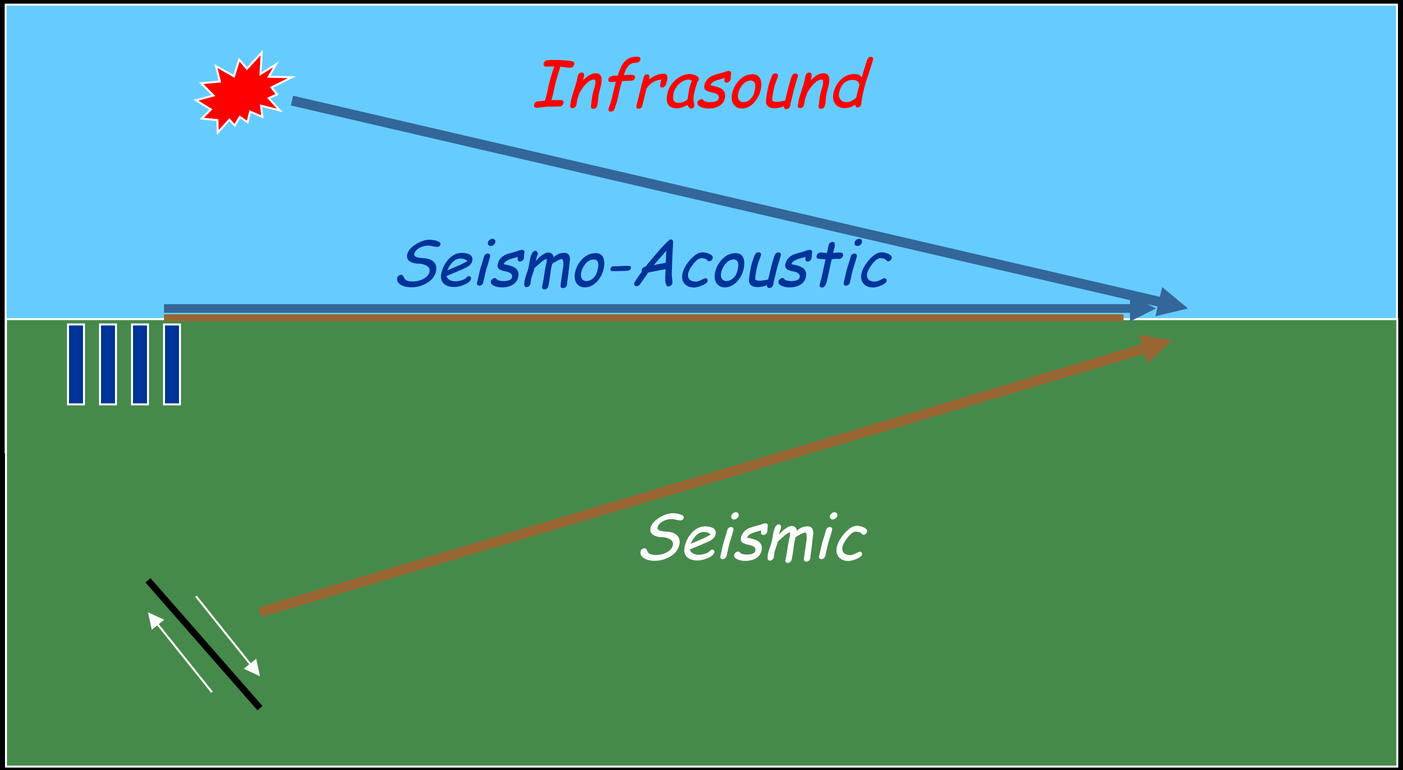

- Natural and man made sources at regional distances
- Seismic and infrasound propagation

Example Explosion the Solid Earth - Atmosphere Boundary

Missile destruction by explosion ~ 50,000 lbs

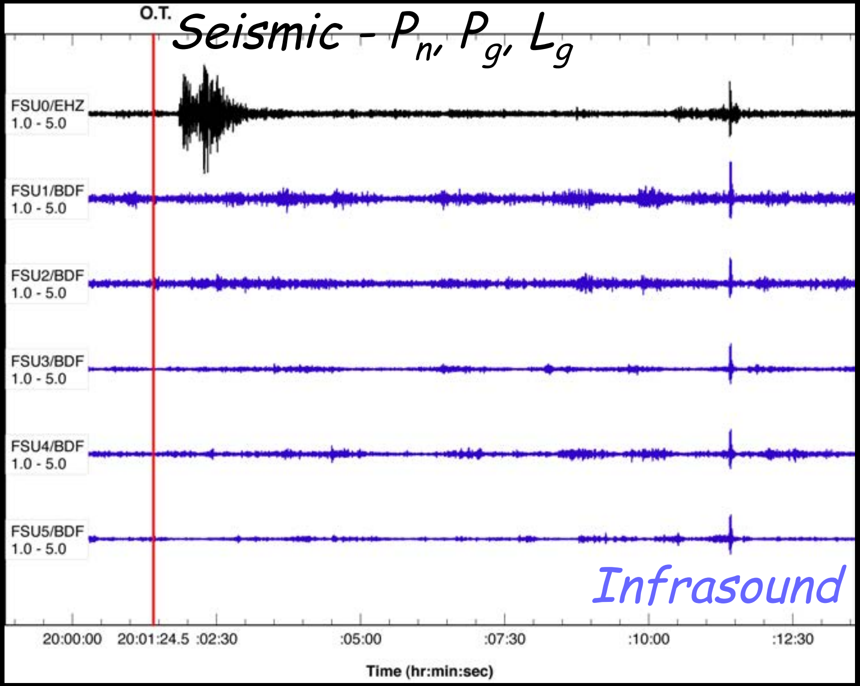

FSU - 160 km
Order of magnitude difference in Propagation Velocity

Overview

- History
- Propagation and the Atmosphere
- Instrumentation and Arrays
- Infrasound Sources
- Combining Seismic and Infrasound
- Large-N Demo

Krakatoa, 1883

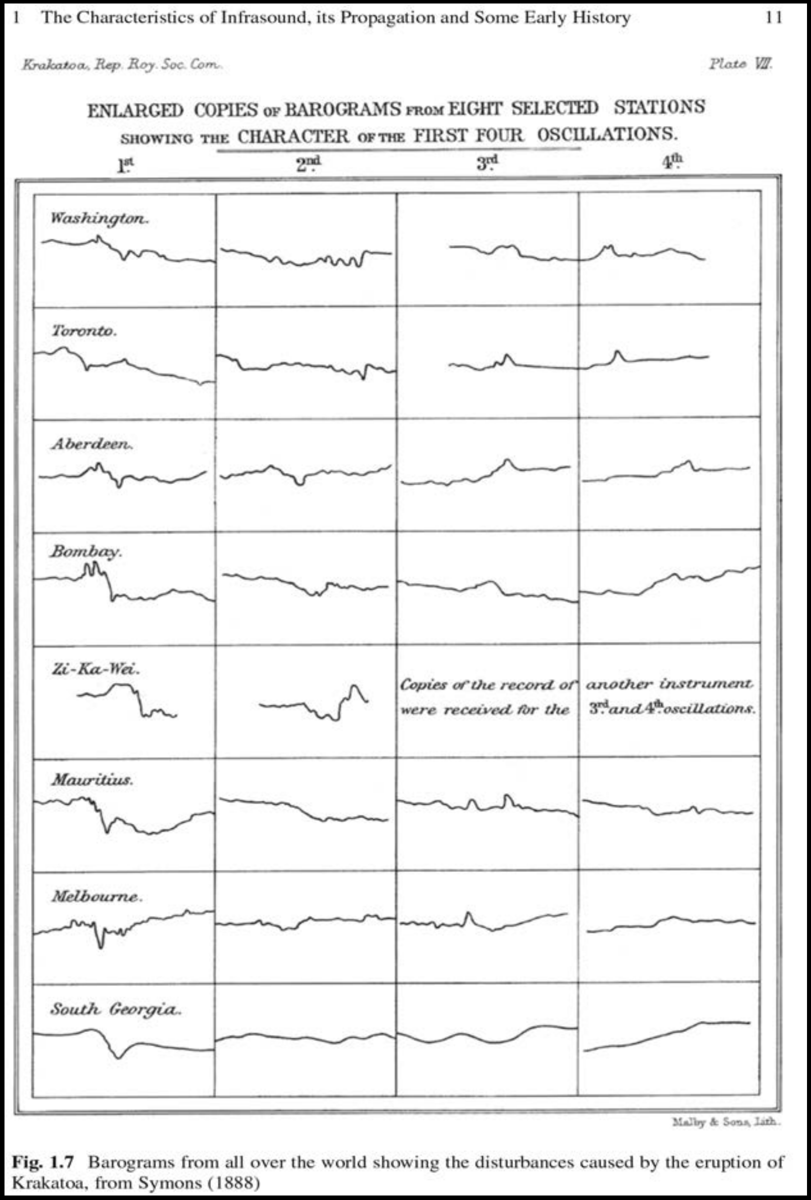

Fig. 1.7 Barograms from all over the world showing the disturbances caused by the eruption of Krakatoa, from Symons (1888)

Evers and Haak, 2010

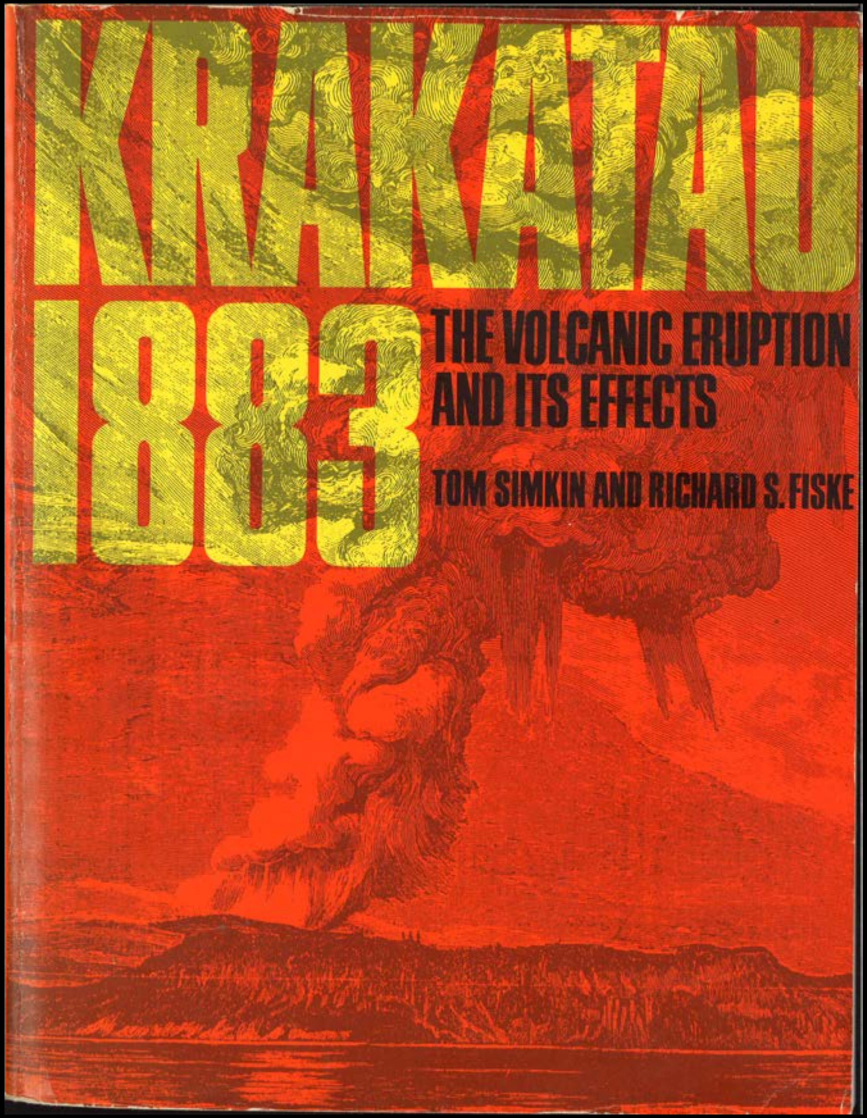

Simpkin and Fiske, 1983.

History

WWI Sounding

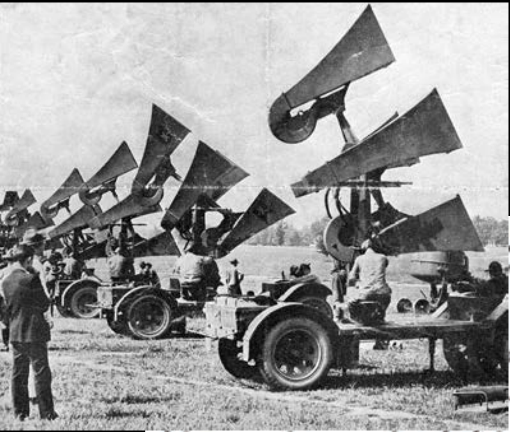

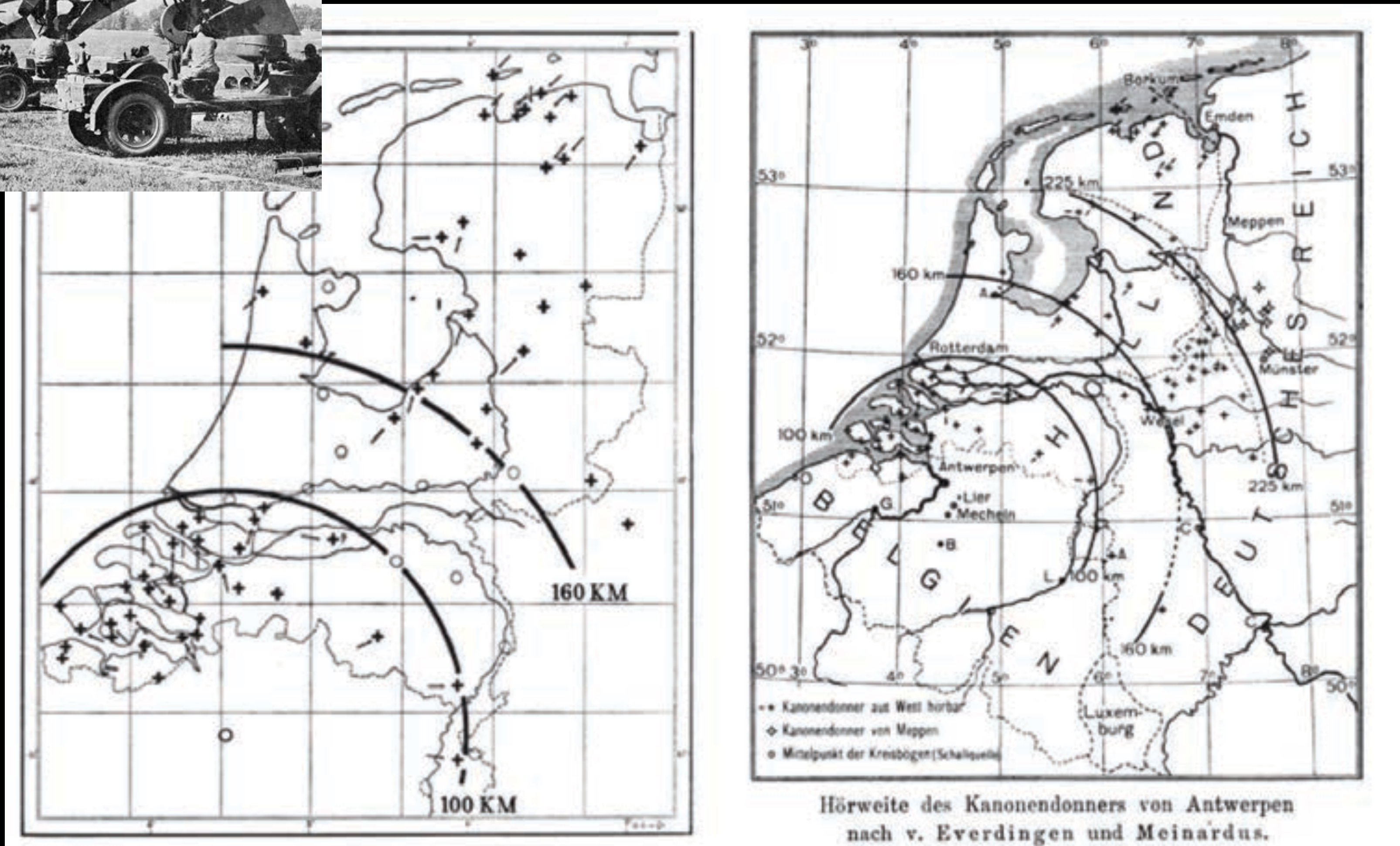

Fig. 1.11 Observations (*crosses*) from canon fires from the siege of Antwerp (*circle*) in the Netherlands (*left*) (Van Everdingen 1914) and Germany (*right frame*) (Meinardus 1915)

Evers and Haak, 2010

History

Monitoring Atmospheric Nuclear Explosions

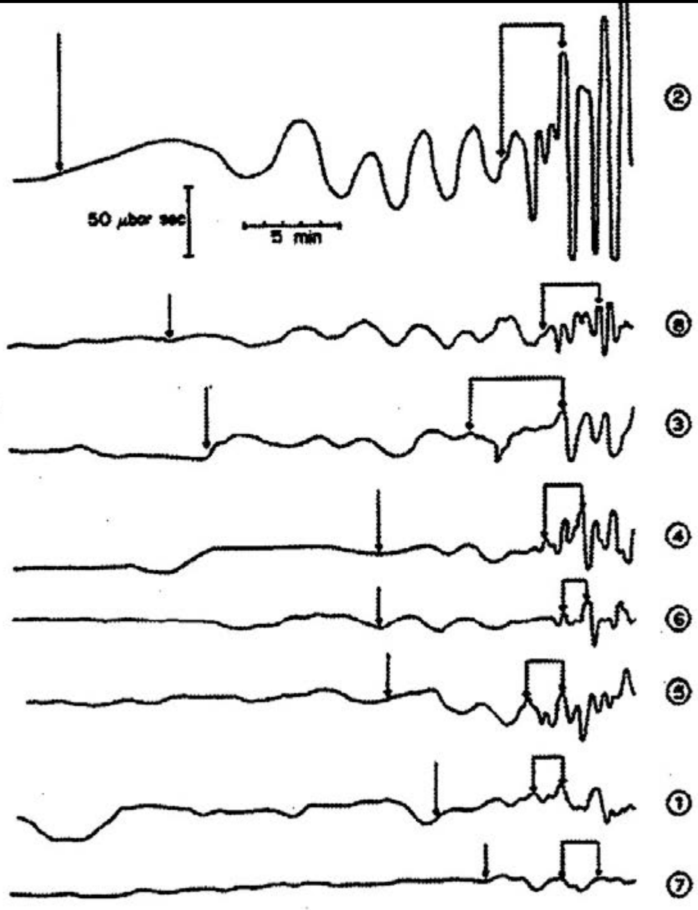

Figure 190. The earliest arrivals of the French Nuclear tests listed in Table 10. The waveforms are listed vertically in the order of decreasing apparent explosive yield. Increasing time runs from right-to-left. [Figure adopted from *Flores and Vega* (1975).]

McKisic, 1997

History

Comprehensive Nuclear Test Ban Treaty - 1996

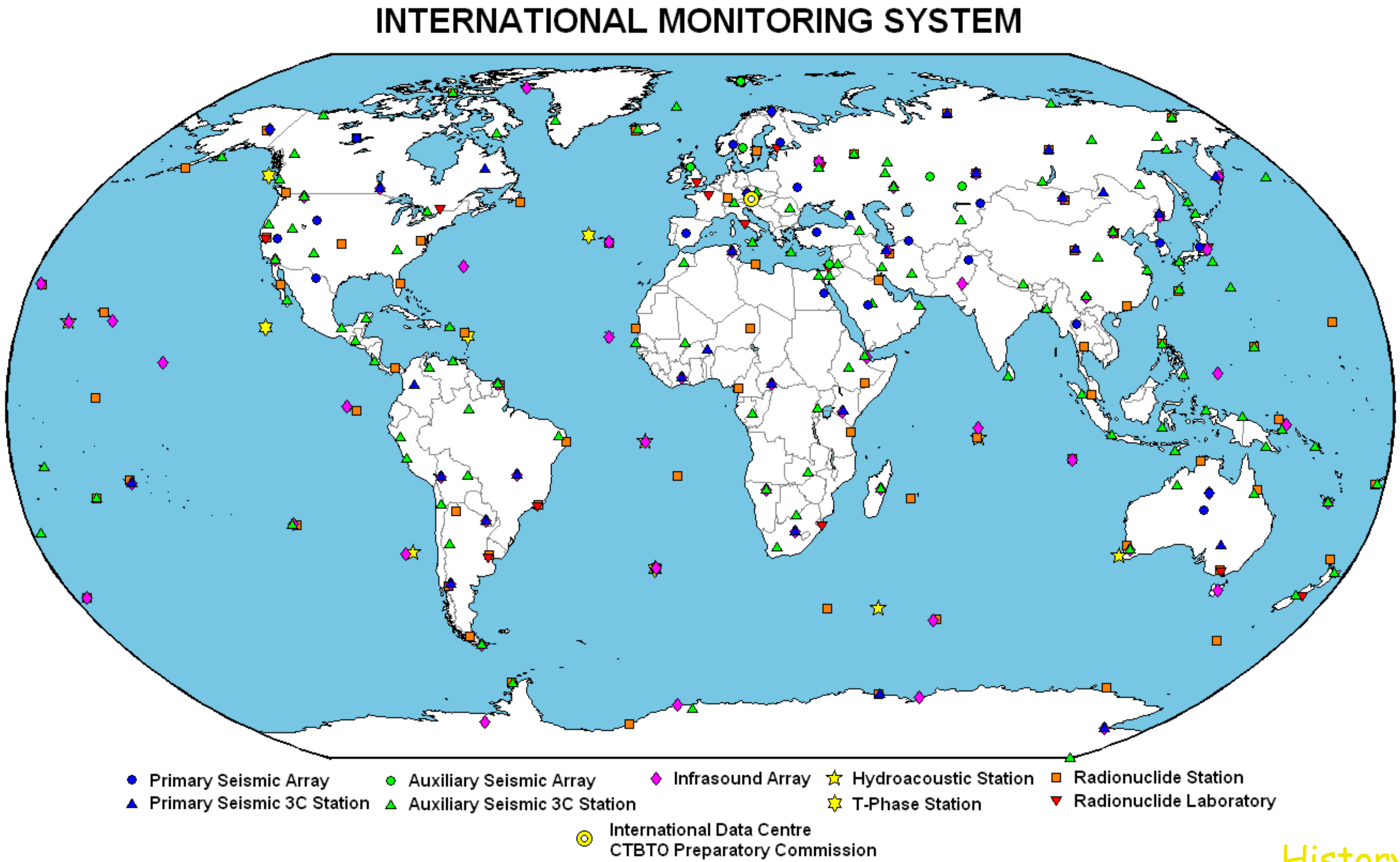

History

Types of Infrasound Arrivals

RG4003 Arrowsmith et al.: SEISMOACOUSTIC WAVEFIELD RG4003

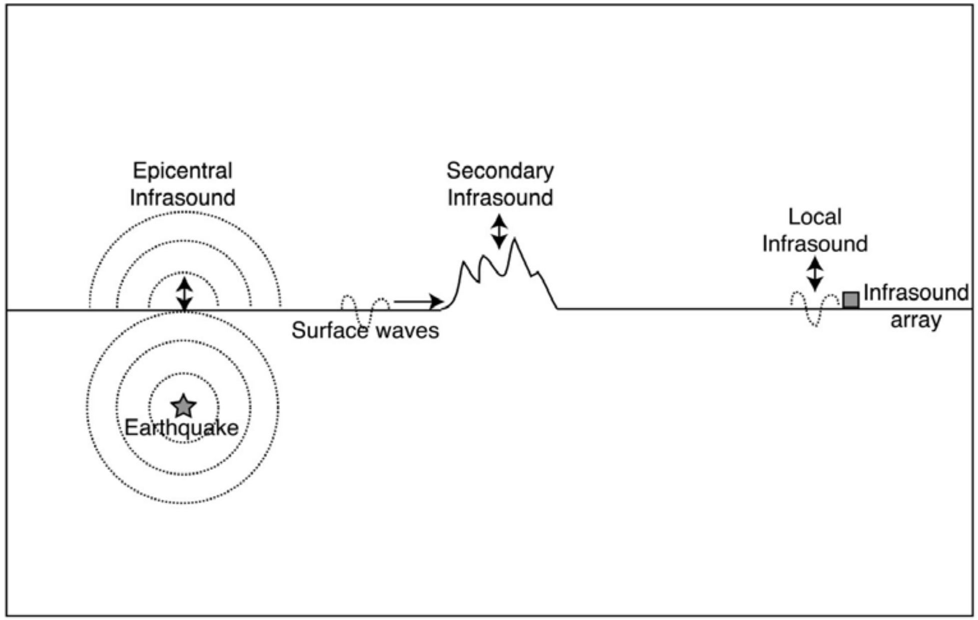

Figure 2. Cartoon illustrating the generation of seismoacoustic signals from earthquakes, which occurs via a variety of interactions between mechanical waves in the crust and atmosphere.

$$\lambda = \frac{V}{f} = V \cdot T$$

- Seismic and Infrasound frequency (f) bands similar (1-10 Hz)
- Infrasound velocities are at least 10 times slower than seismic ~ 330 m/s
- Infrasound Wavelengths are at least 10 times shorter (10s-100s m)

Arrowsmith et al., 2010

Atmospheric Path Effects - Temperature

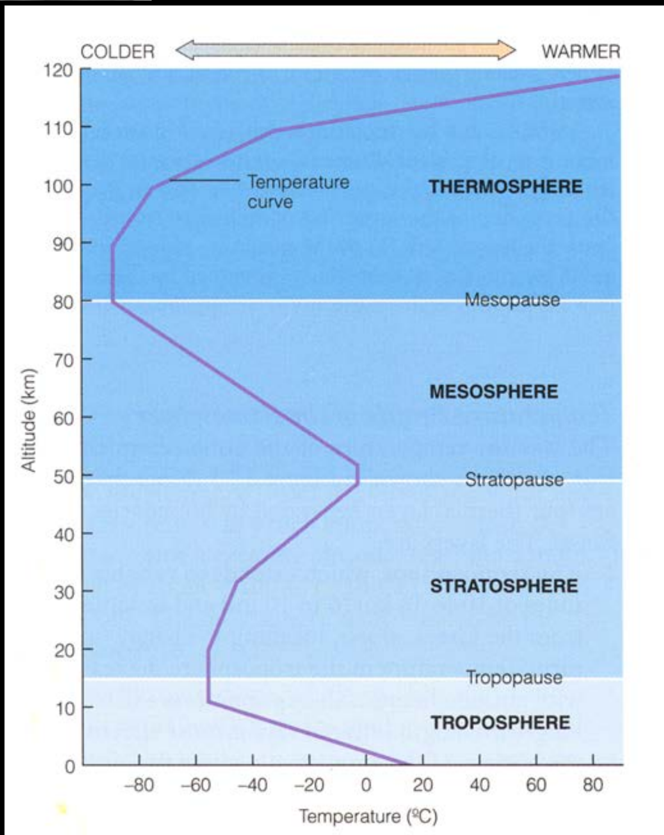

Skinner, Porter and Botkin, 1999

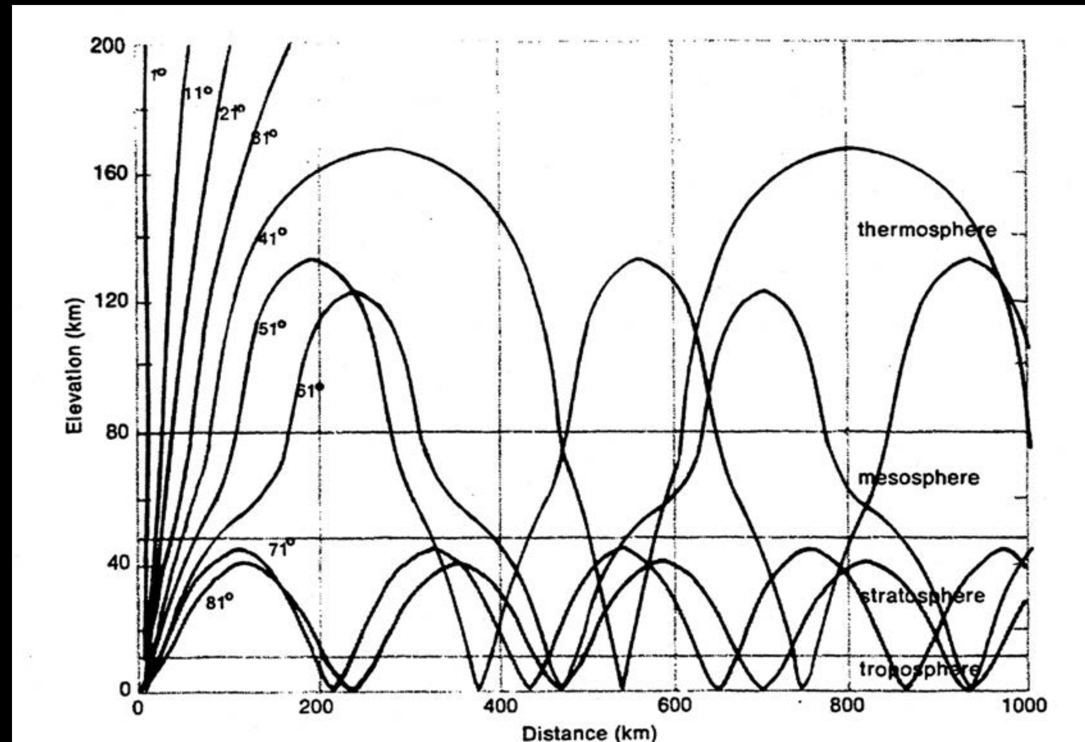

Figure 4. Ray paths for a sound source on the ground to a range of 1000 km including both stratospheric and ionospheric reflections. [Figure adopted from *Donn* (1978).]

$$c = \left(\frac{\gamma R T}{M}\right)^{1/2}$$

$$c = 20.07\sqrt{T}$$

Atmospheric Path Effects – Plus Wind

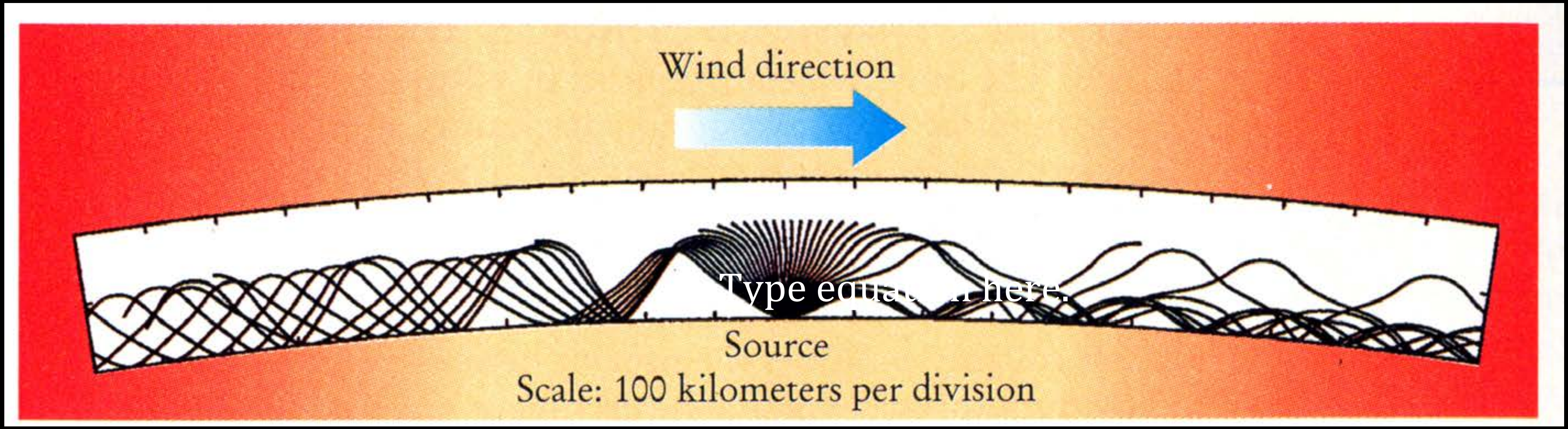

Bedard and Georges, 2000

- *Atmospheric wind direction and velocity perturbs velocity of propagation*
- *Weather patterns can introduce propagation ducts*
- *Propagation model is time dependent*

$C_{eff} = C_T + \mathbf{n} \cdot \mathbf{v}$

C_T: velocity from temp

n: direction of prop

v: velocity of wind

Winds Parallel to Propagation

RG4003 Arrowsmith et al.: SEISMOACOUSTIC WAVEFIELD RG4003

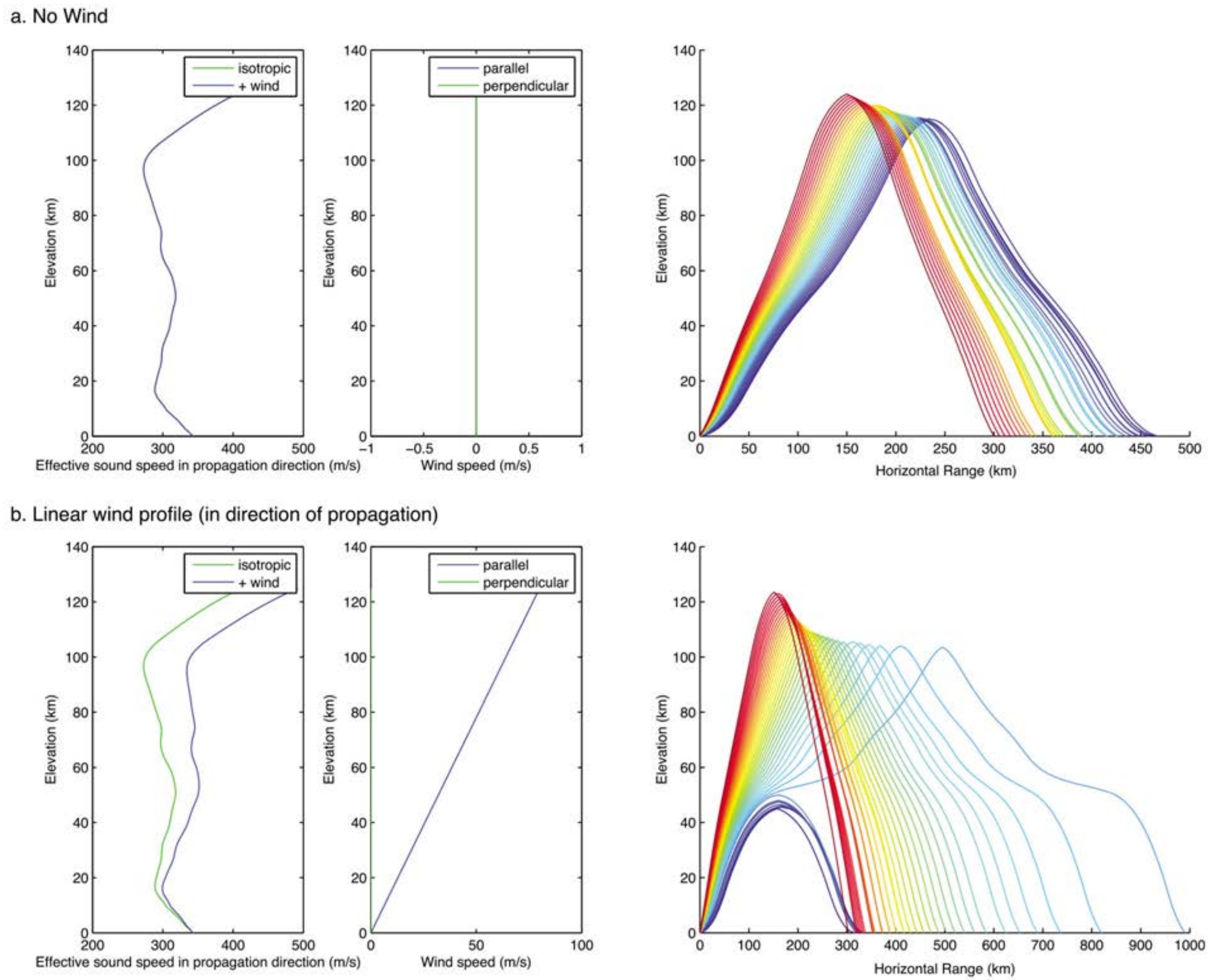

Figure 7. Tau-P simulations showing the effect of wind in the direction of propagation. Refractions occur in the thermosphere in both cases, but the addition of wind enhances the stratospheric duct.

$$C_{eff} = C_T + \mathbf{n} \cdot \mathbf{v}$$

Arrowsmith et al., 2010

Winds Perpendicular to Propagation

RG4003 Arrowsmith et al.: SEISMOACOUSTIC WAVEFIELD RG4003

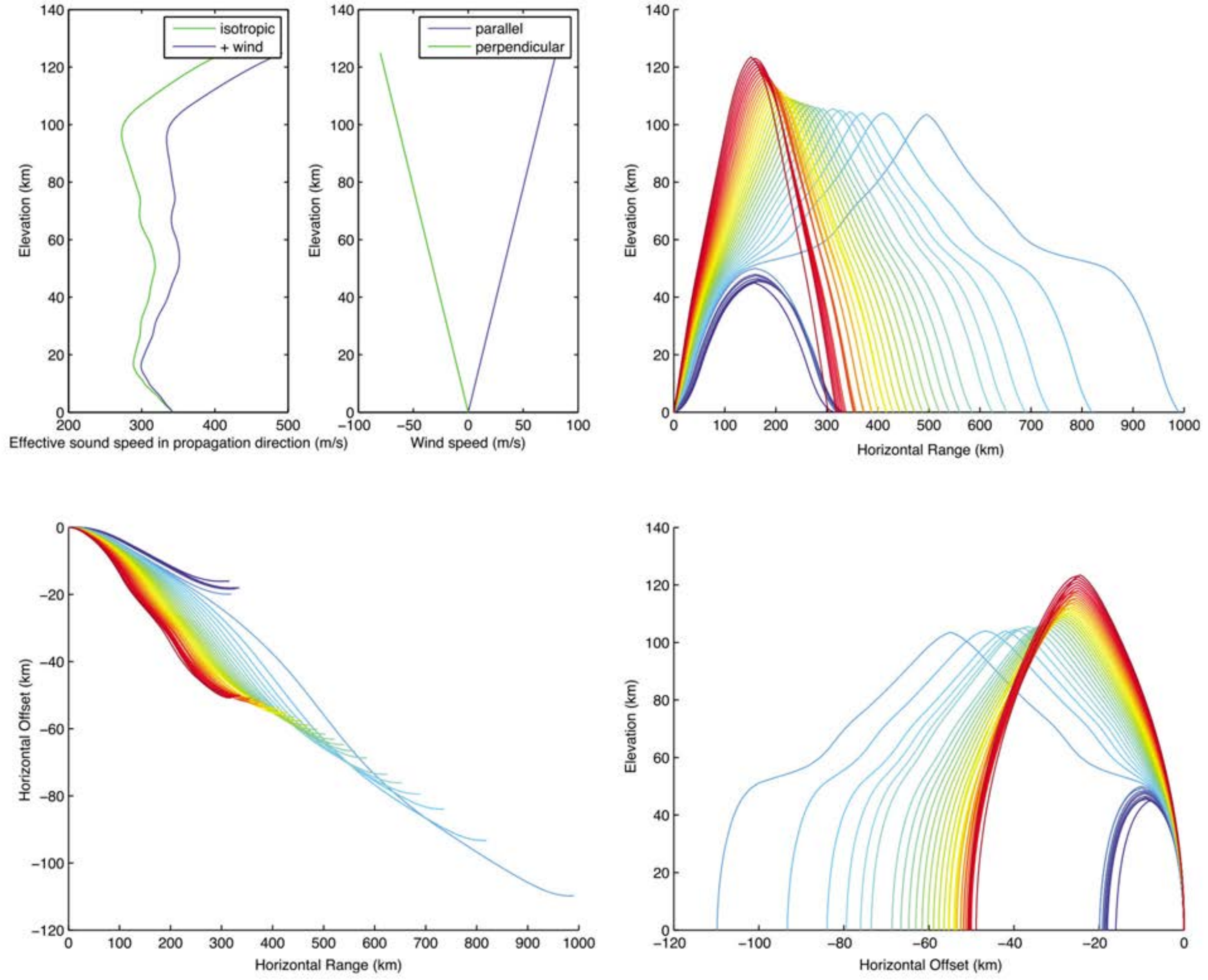

Figure 8. Tau-P simulations showing the effect of wind perpendicular to the direction of propagation.

$$C_{eff} = C_T + \mathbf{n} \cdot \mathbf{v}$$

Arrowsmith et al., 2010

Zone of Silence ?

RG4003 Arrowsmith et al.: SEISMOACOUSTIC WAVEFIELD RG4003

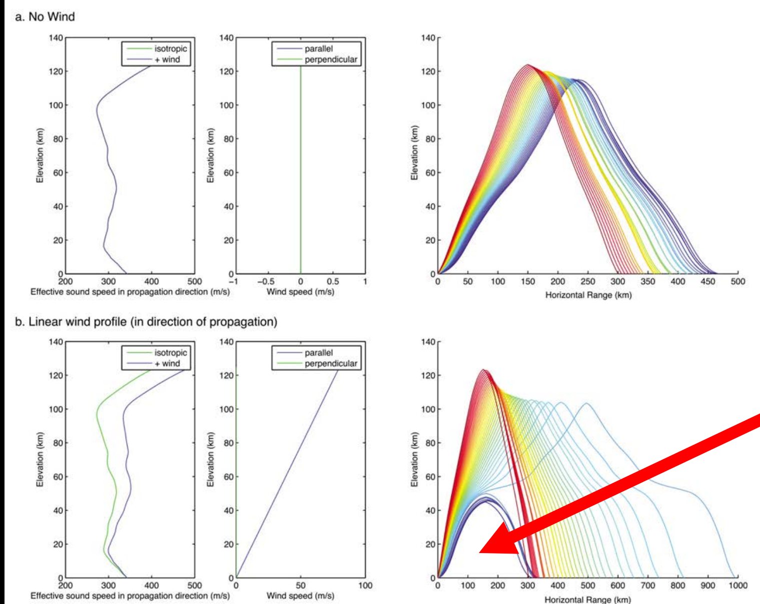

Figure 7. Tau-P simulations showing the effect of wind in the direction of propagation. Refractions occur in the thermosphere in both cases, but the addition of wind enhances the stratospheric duct.

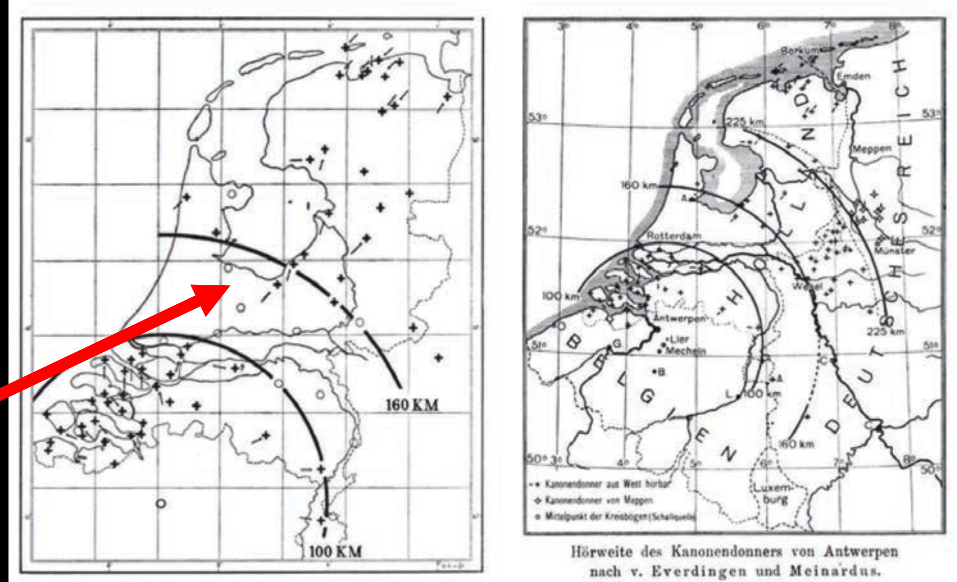

Fig. 1.11 Observations (*crosses*) from canon fires from the siege of Antwerp (*circle*) in the Netherlands (*left*) (Van Everdingen 1914) and Germany (*right frame*) (Meinardus 1915)

Arrowsmith et al., 2010

Propagation & Atmosphere

Primary Focus on Two Complementary Paths

Zone of Silence?

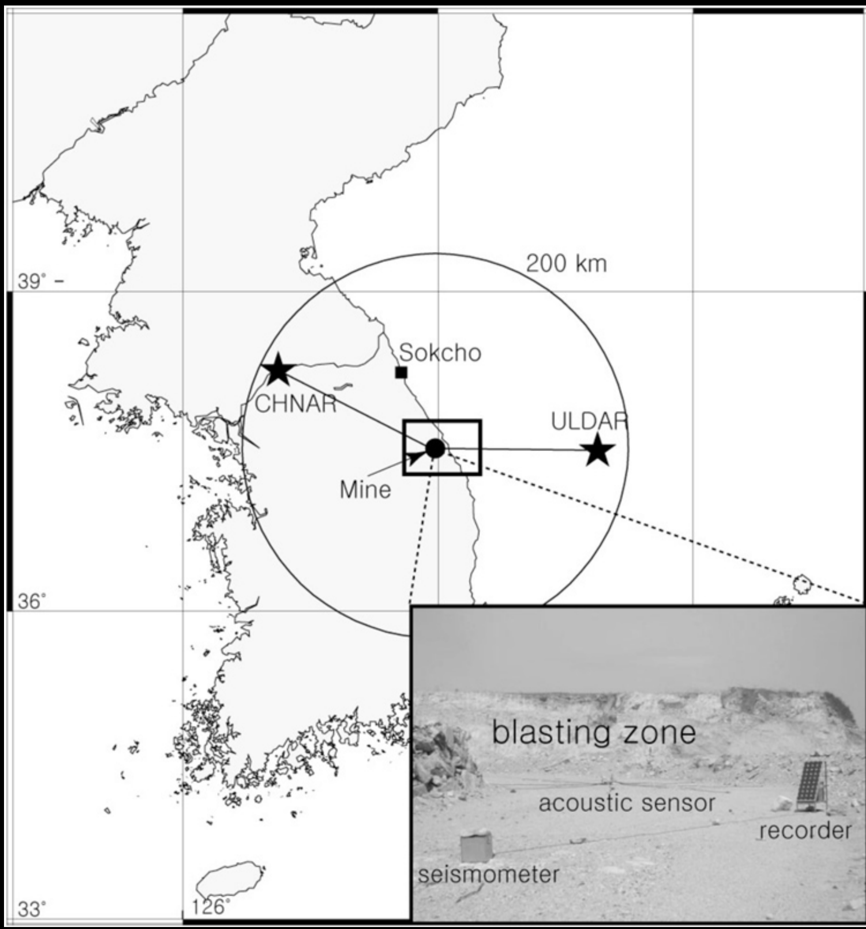

Origin time and location constrained by in-mine instrumentation

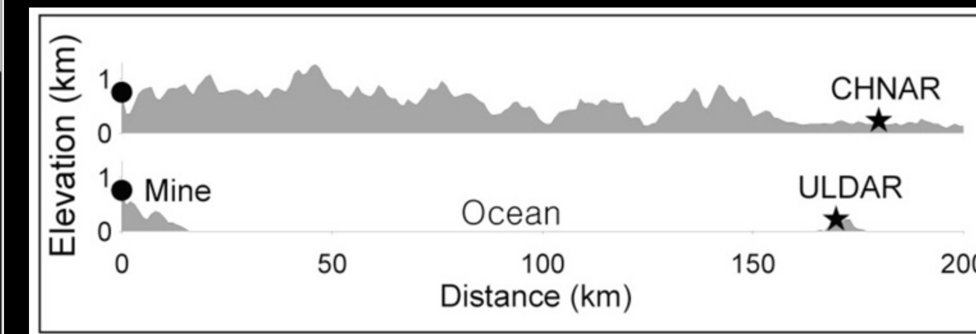

Two arrays are 181 km (CHNAR) and 169 km (ULDAR) from mine along one continental path and one oceanic path

Che et al., 2011

Seasonal Variations in Travel-Times and Backazimuths

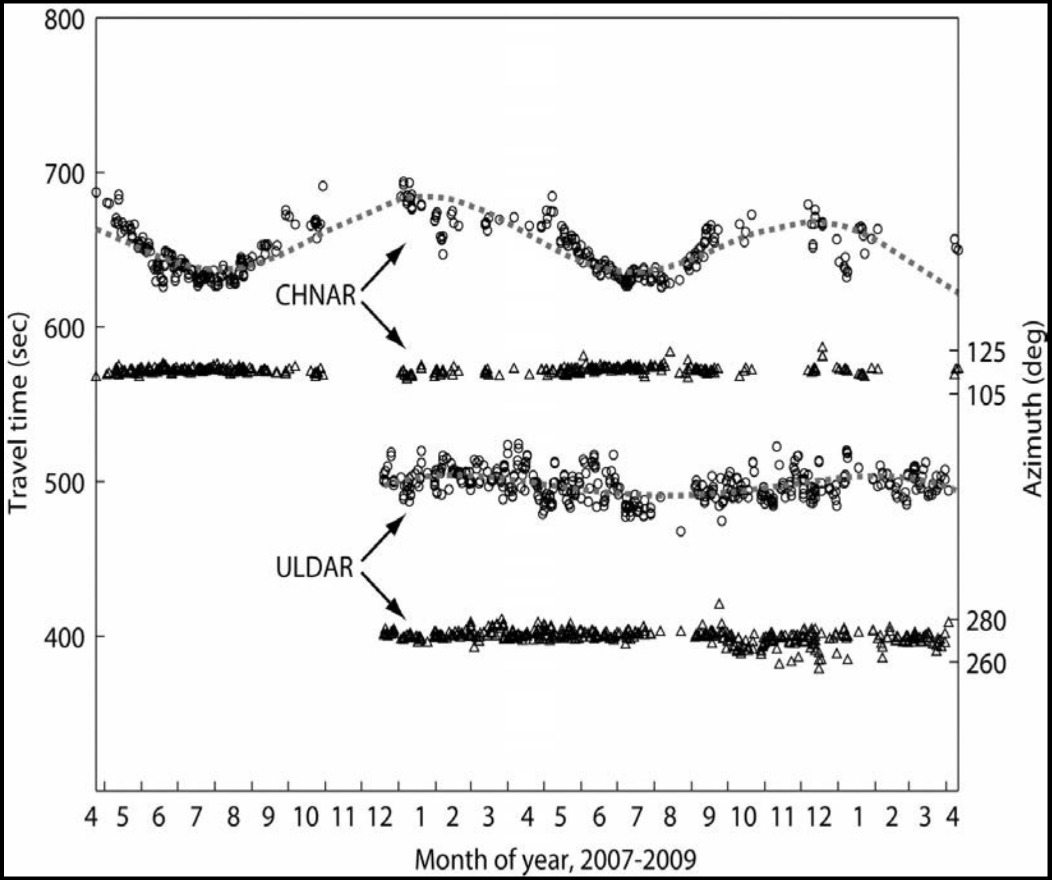

CHNAR 260 to 289 m/s, characteristic of stratospheric returns

ULDAR 322 to 361 m/s, characteristic of stratospheric returns

- Strong seasonal variation in travel time to CHNAR
- Larger variation in travel-times to ULDAR (much faster)
- Small variation in backazimuth
- Seasonal Detectability

Che et al., 2011

Ray Tracing 2007-2009

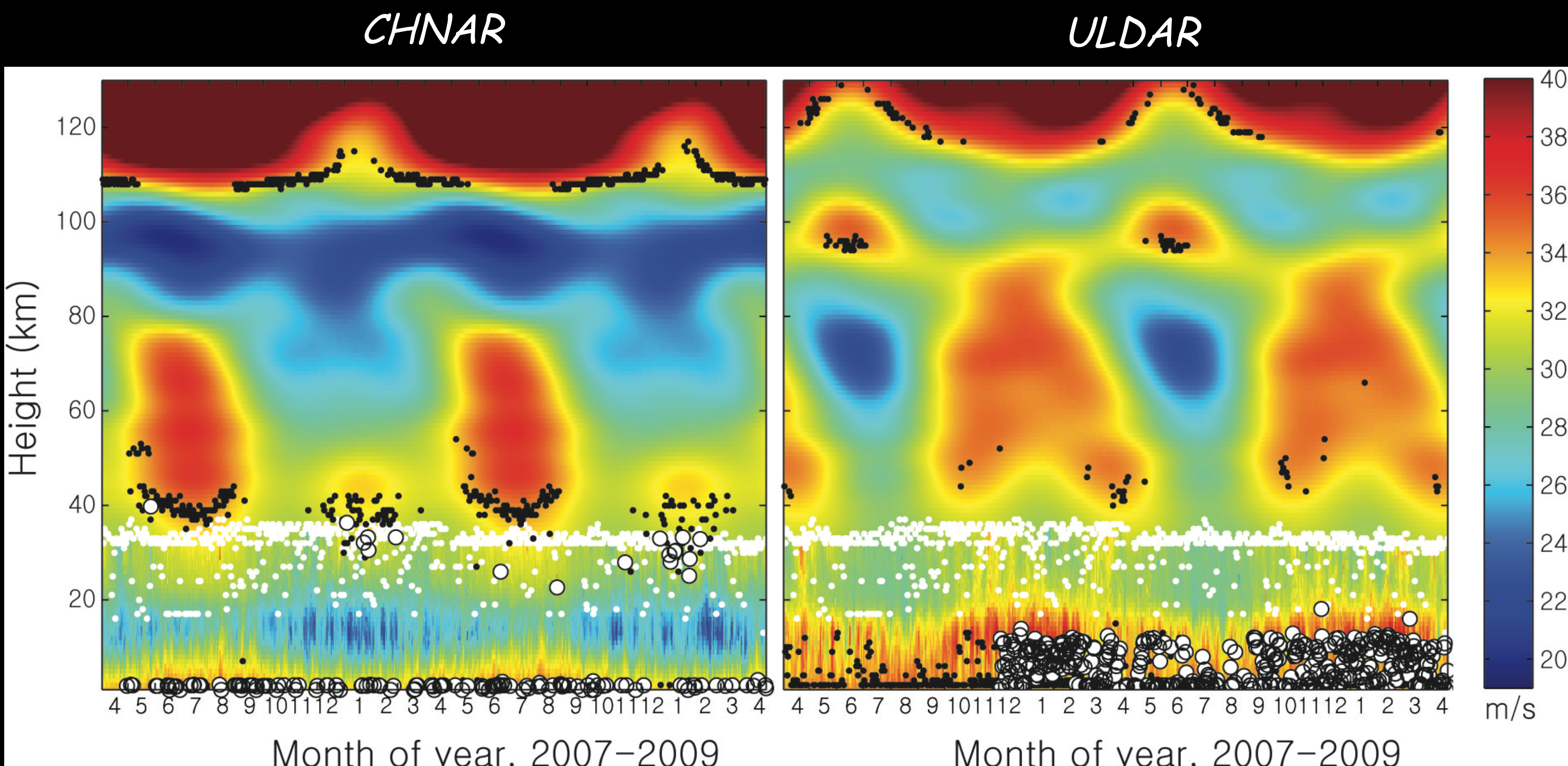

- White Dots – Height of Balloon Data
- Black Dots – Height where atmospheric velocity is higher than velocity at surface
- White Circles – Turning points in atmosphere of predicted eigenrays

Che et al., 2011

Seasonal Variation of Zonal Winds

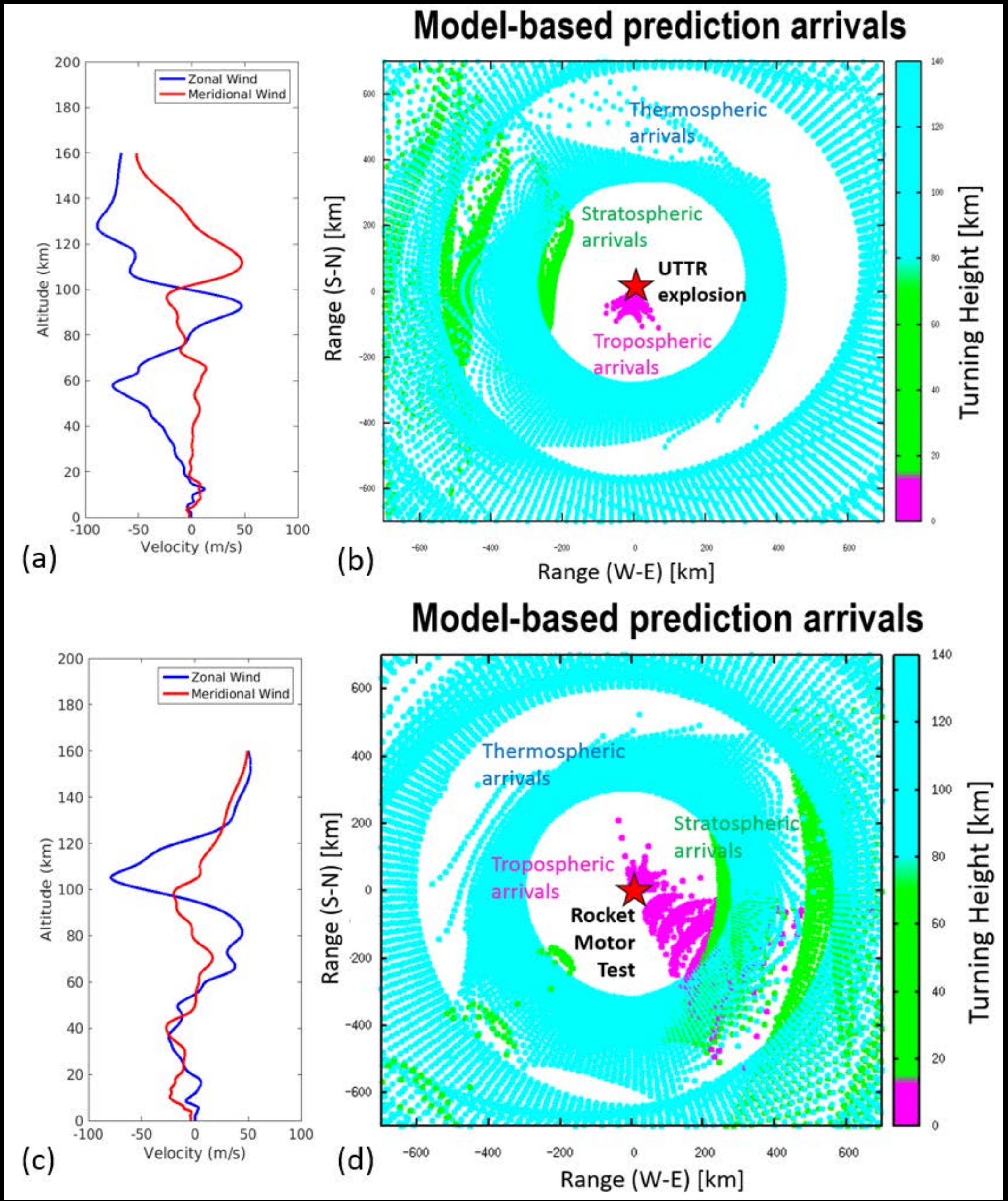

Summer

Winter

Observations

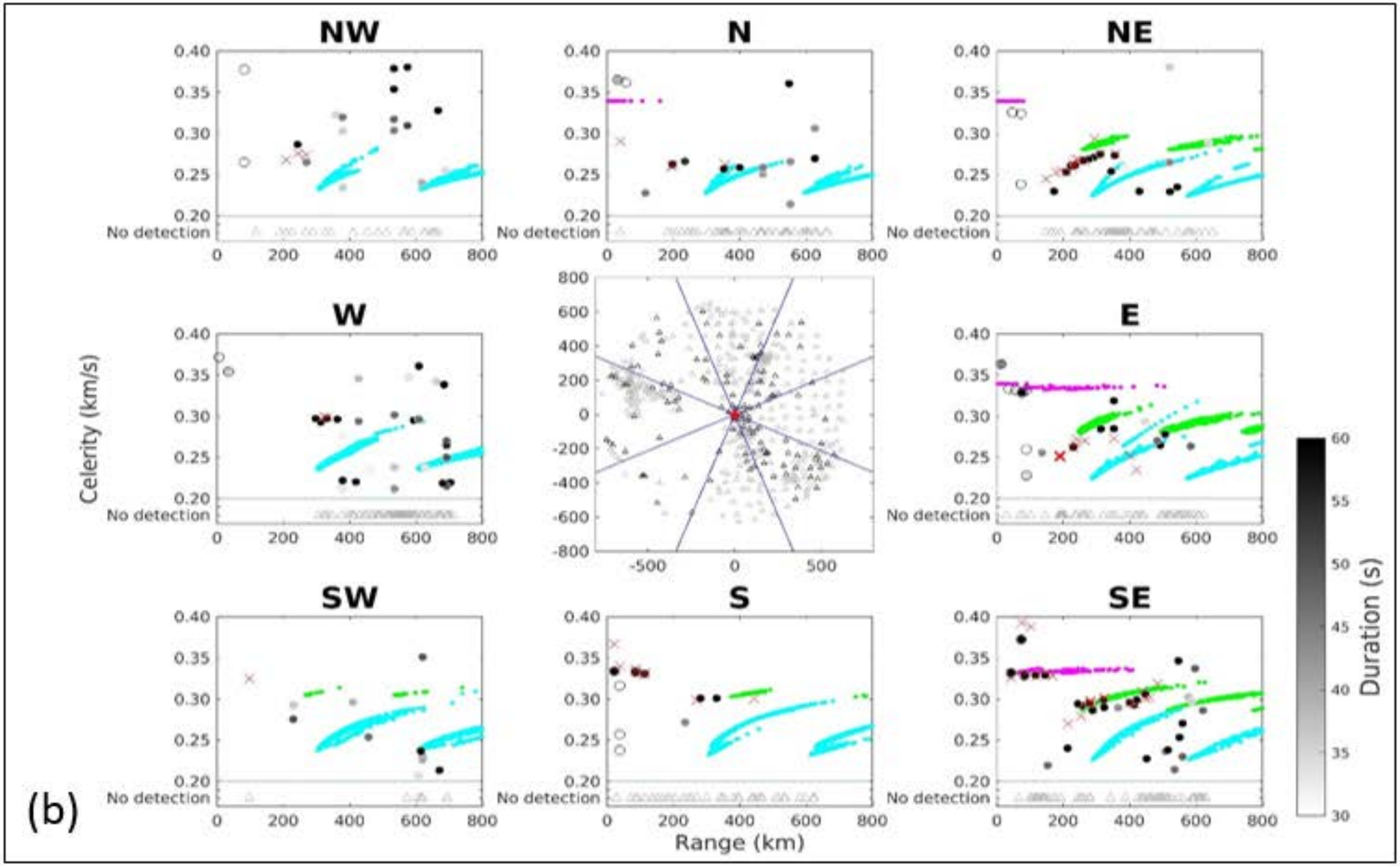

Winter

Observations

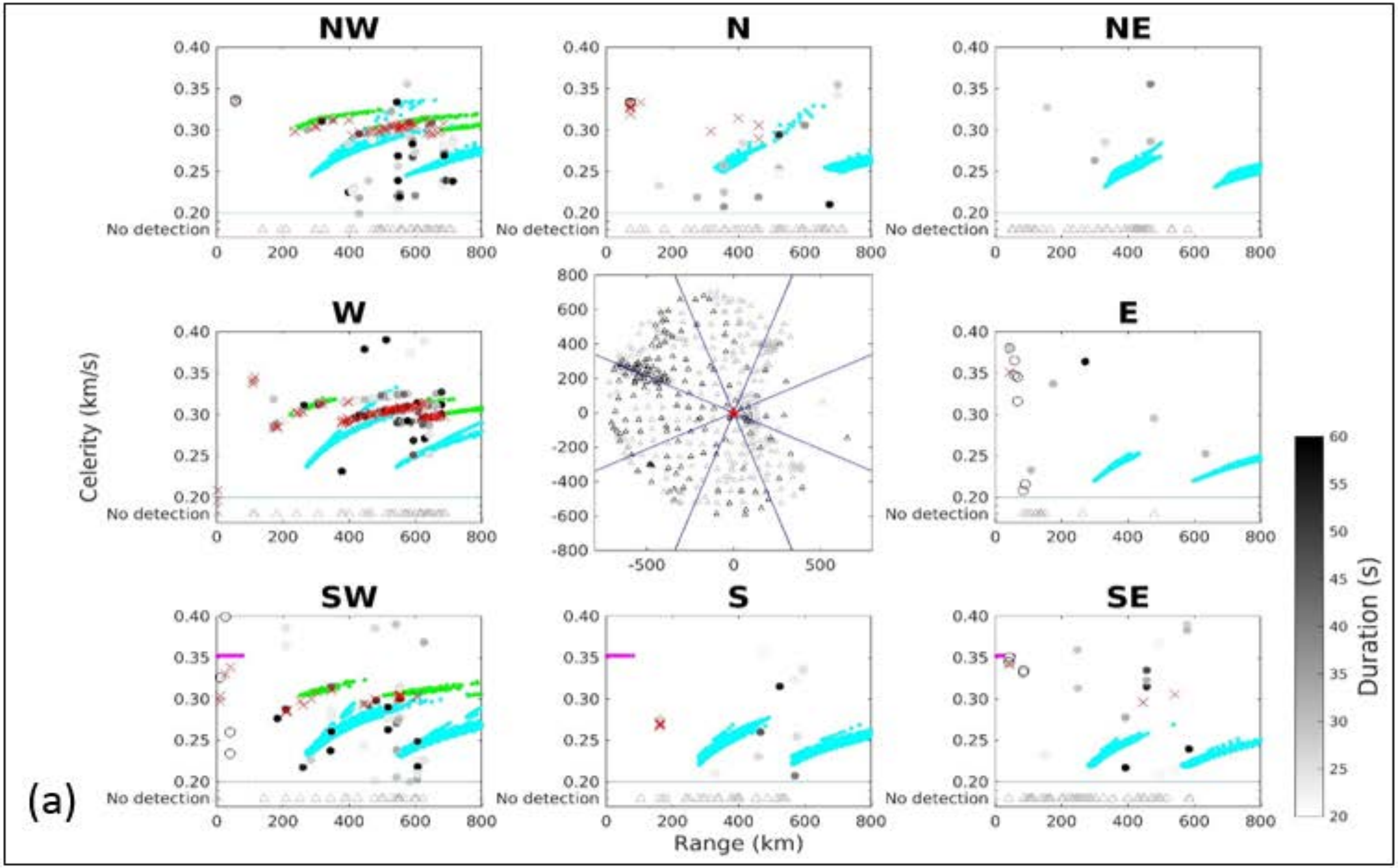

Summer

Seismometers Capture Infrasound

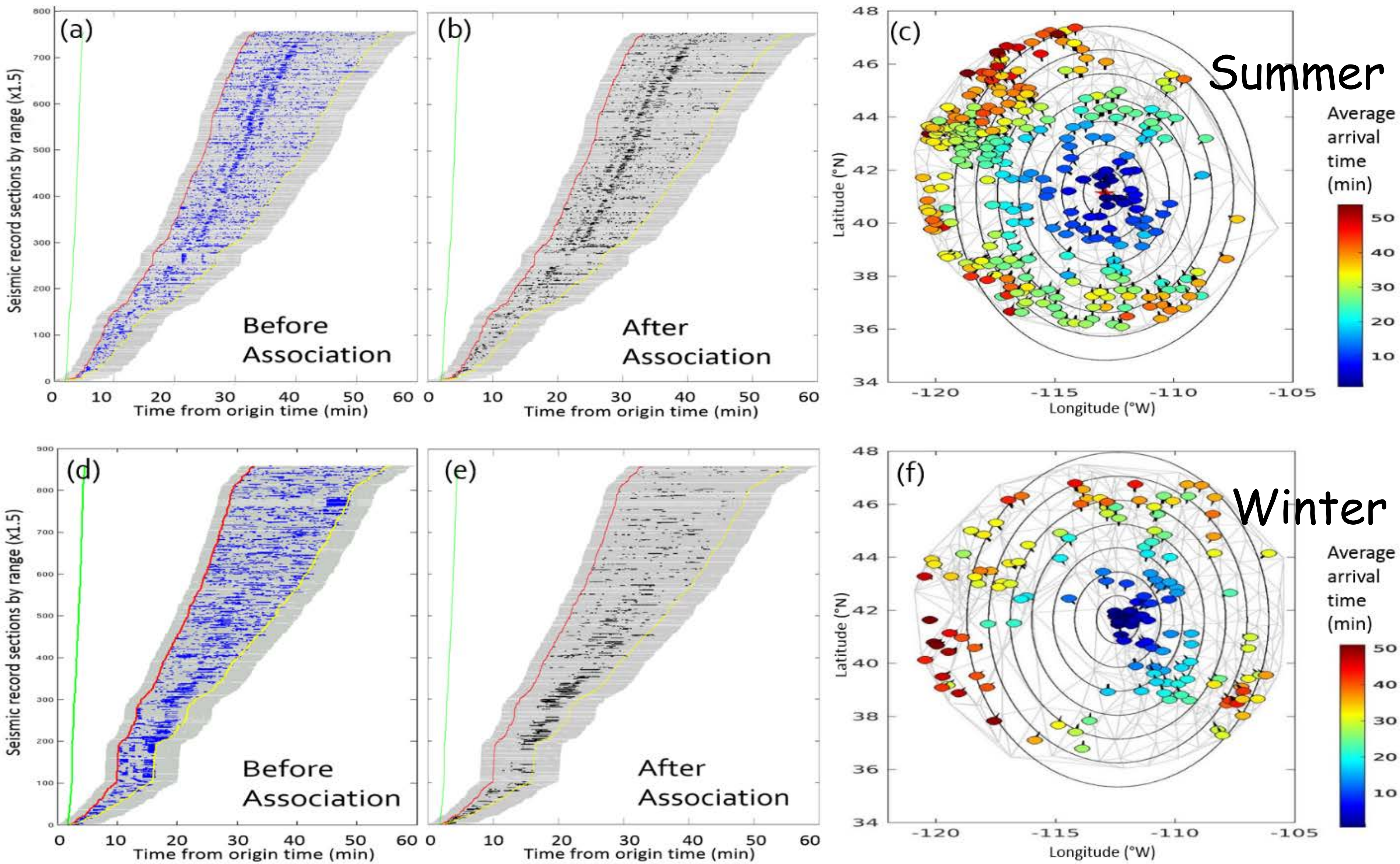

Integrated Seismo-Acoustic Array

SEISMIC

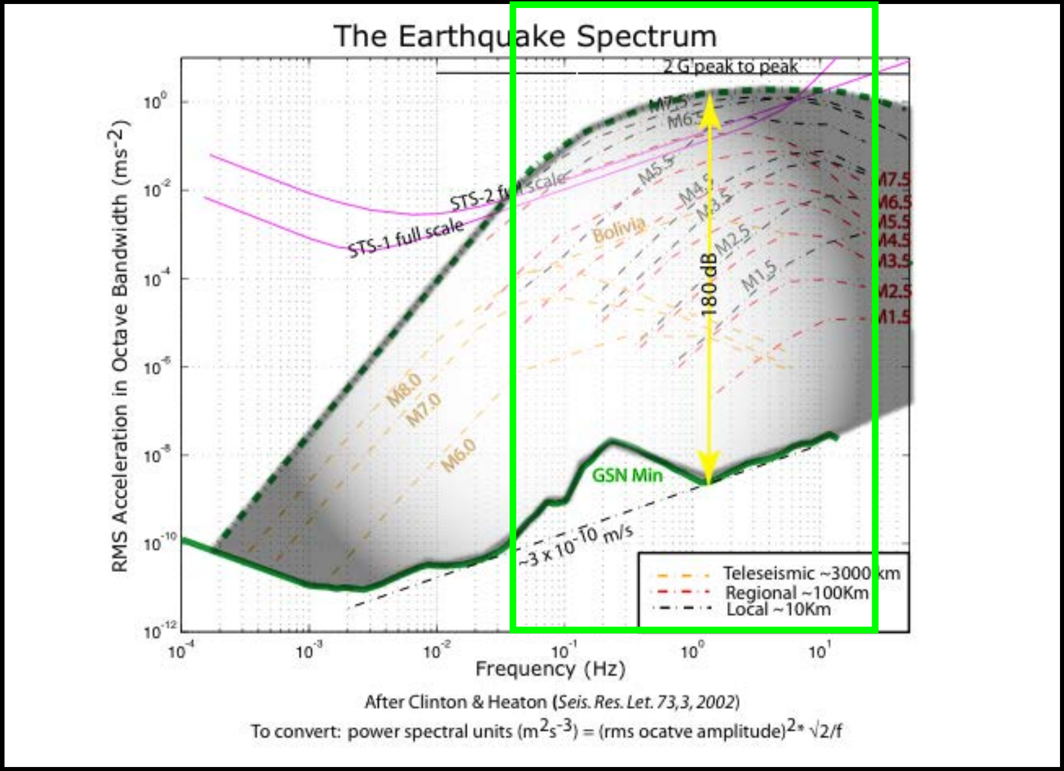

Ingate and Berger, 2005

INFRASOUND

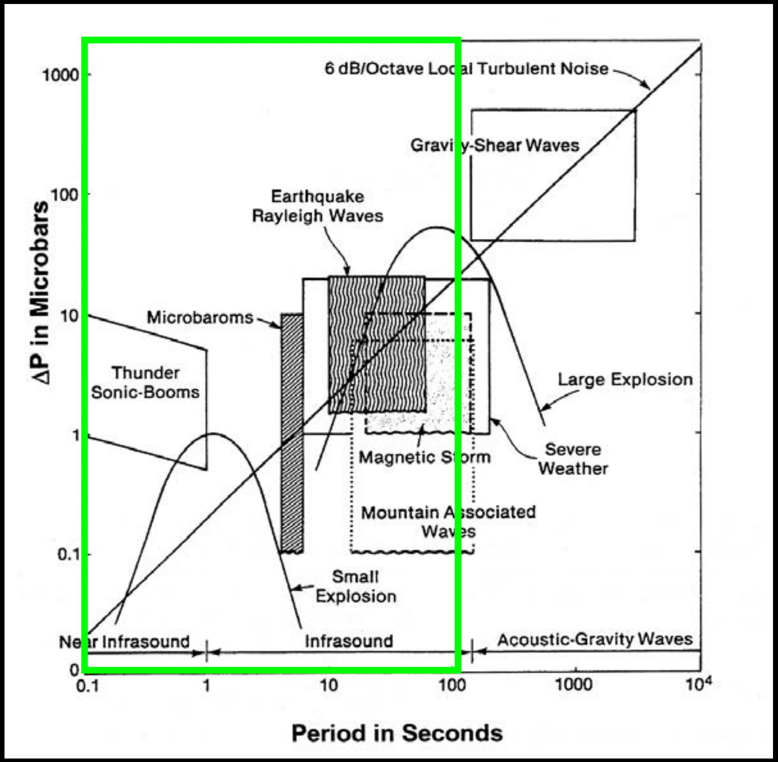

Bedard, 1999

Similar Frequency Bands but Order Magnitude Wavelength Differences

Noise Comparison

SEISMIC

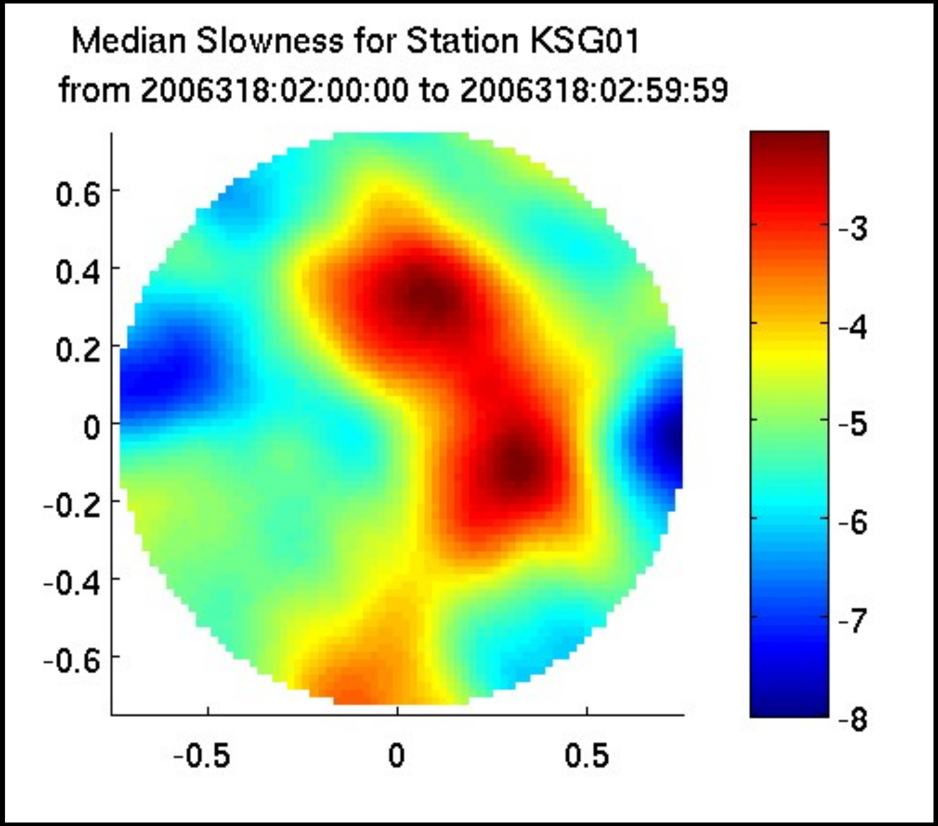

INFRASOUND

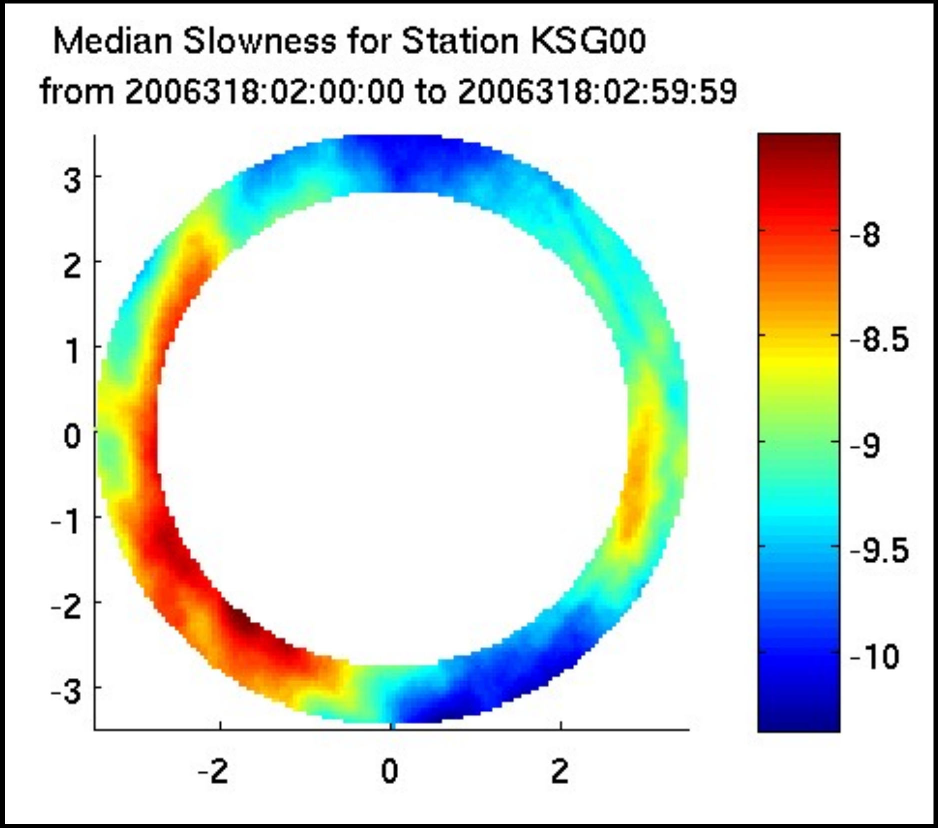

Large Difference in Slowness and Noise Characteristics

Noise and Wind Velocity

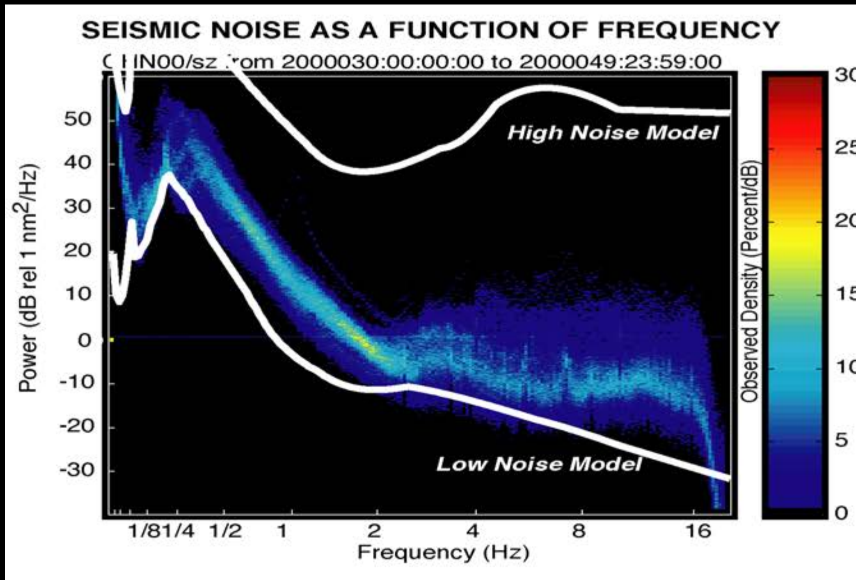

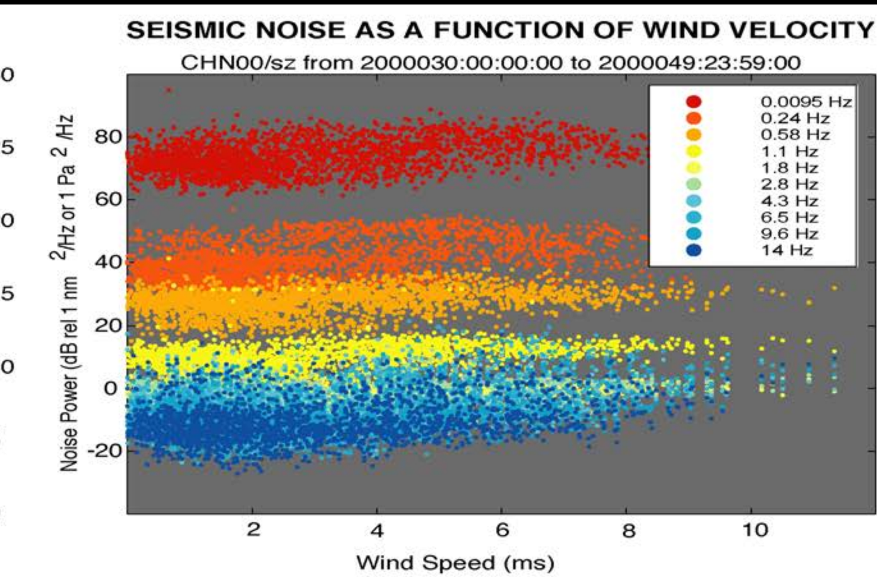

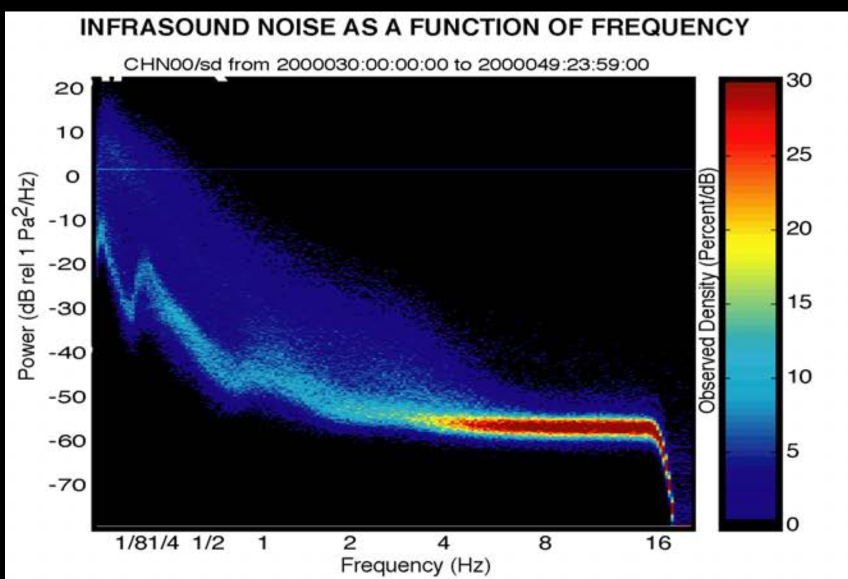

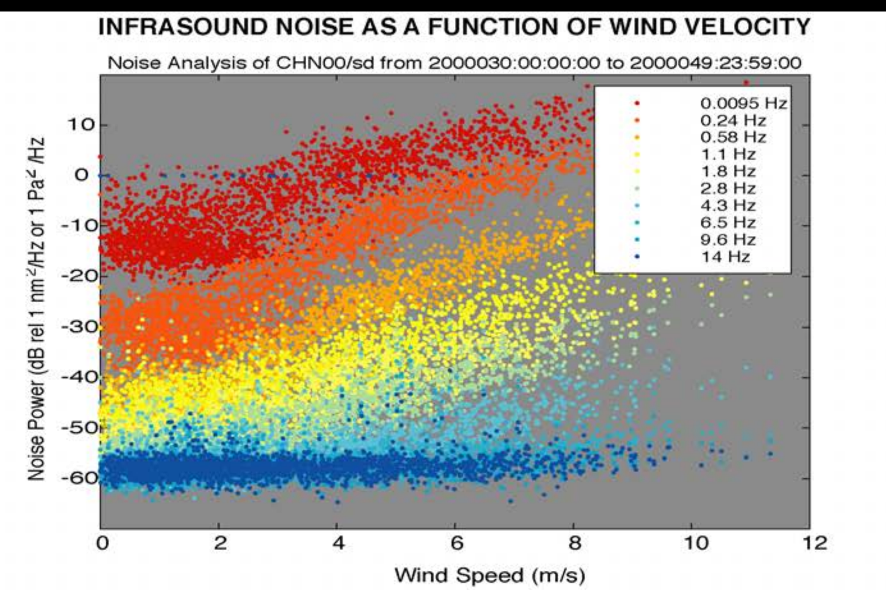

Seismic and Acoustic Characteristics

	Seismic	Acoustic
Scale	km	50 meters
Site	Hard rock	Forest
Incoherent Noise	High wavenumber	Low wavenumbers during wind
Coherent noise	Oriented with seismic sources	Oriented with wind or local sources
Sensor reliability	High	Moderate
Sensor cost	High	Moderate
Installation requirements	Moderate	Low
Array Gain	Moderate	High

Decreasing Incoherent Noise from Turbulence at Free Surface

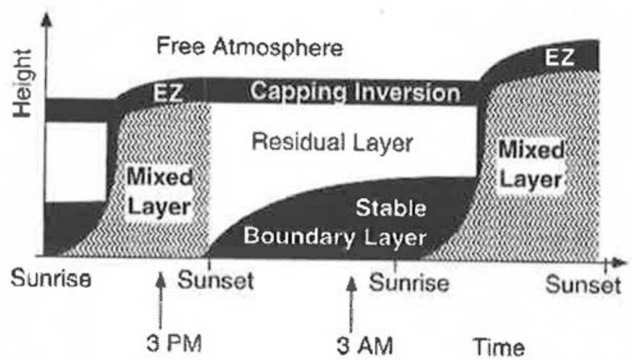

Fig. 1.3. Daily cycle of the structure of the atmospheric boundary layer (Stull 2000), EZ: Entrainment zone

height in m	name		exchange		stability
1000	upper layer (Ekman-layer)		turbulent	no const. flux	influence of stability
20	turbulent layer	surface layer (Prandtl-layer)		flux constant with height	
1	dynamical sublayer				no influence of stability
0.01	viscous sublayer		molecular/ turbulent		
0.001	laminar boundary layer		molecular		

Fig. 1.4. Structure of the atmospheric boundary layer

Foken, 2008

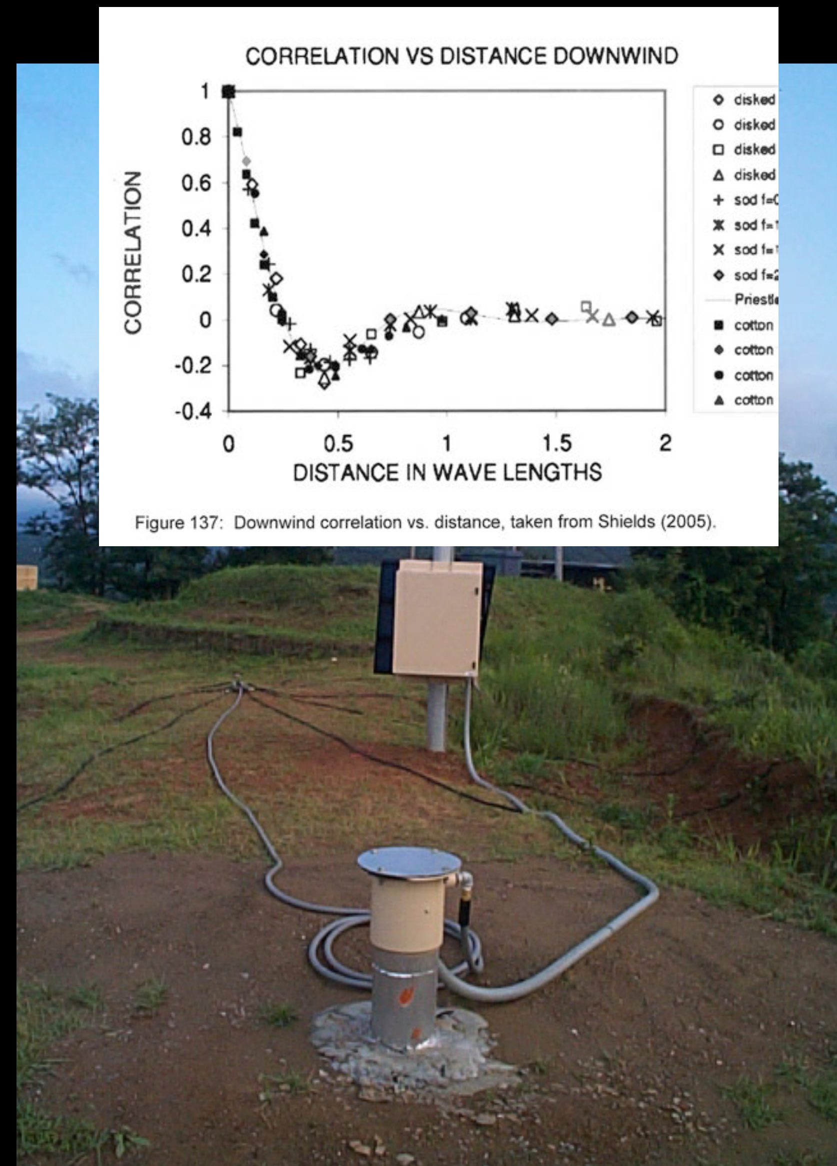

Figure 137: Downwind correlation vs. distance, taken from Shields (2005).

Array Designed for Wavelength Differences

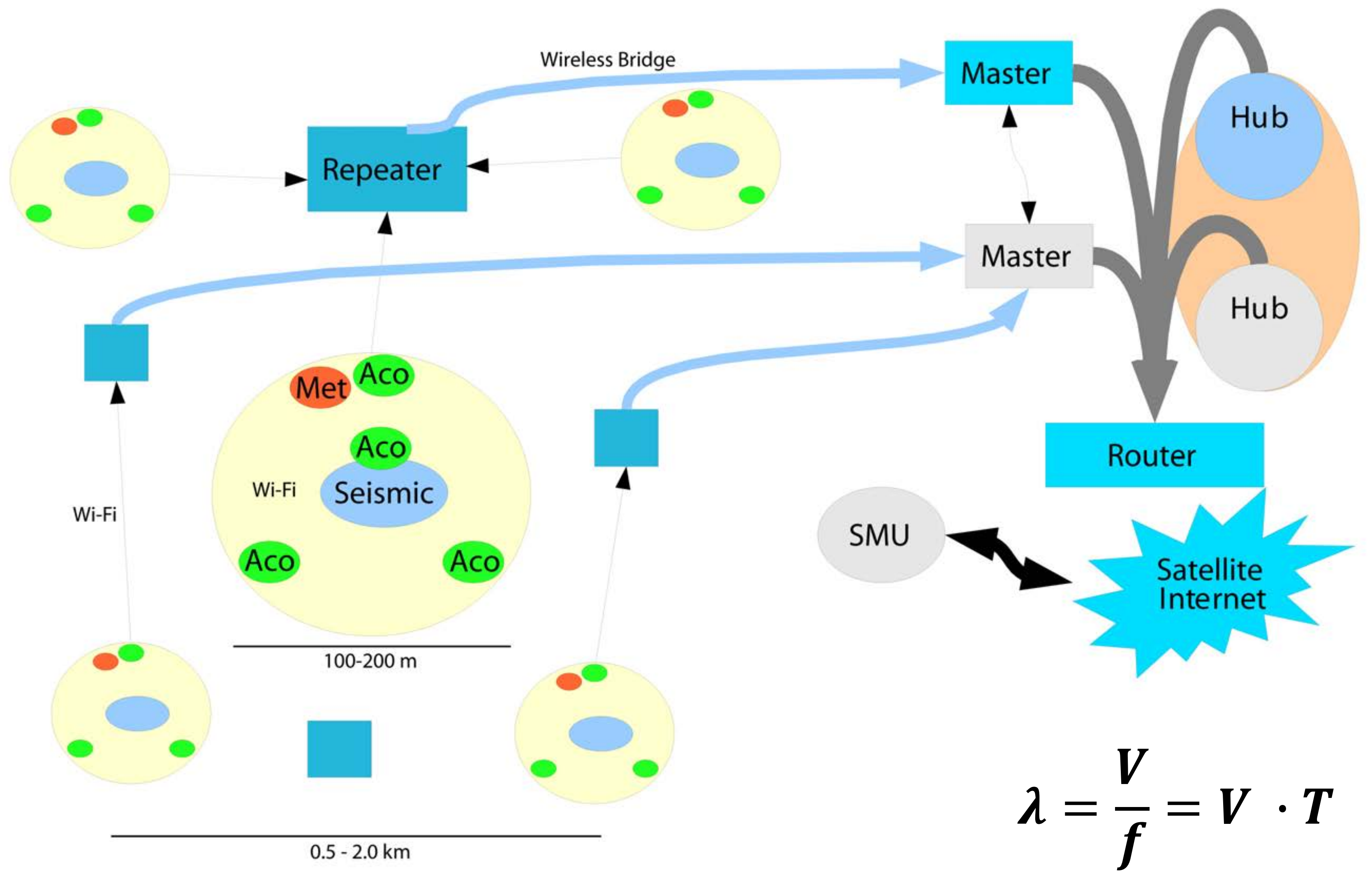

$$\lambda = \frac{V}{f} = V \cdot T$$

Korea Infrasound Network

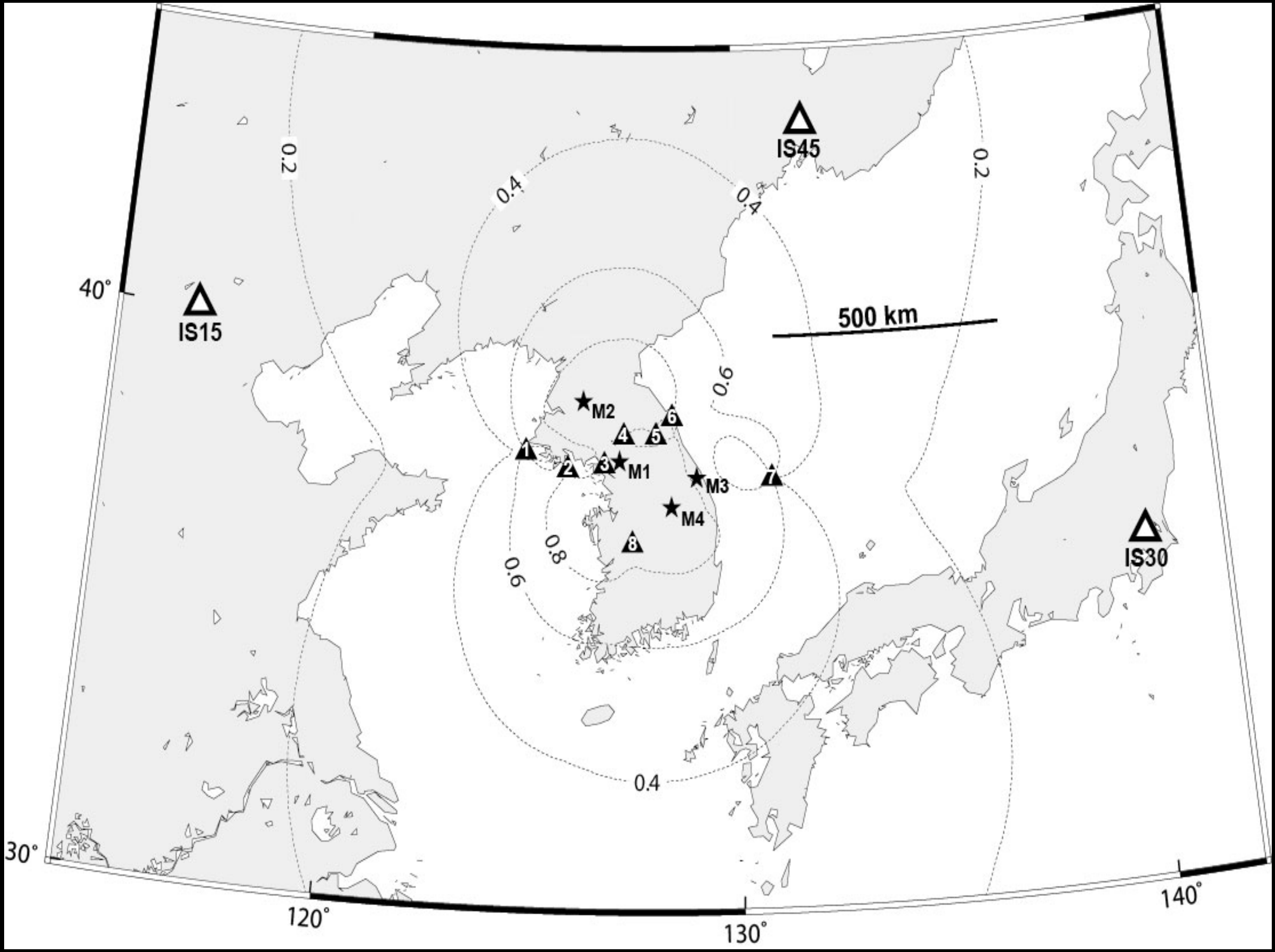

Nearly co-linear station distribution illustrates value of IMS resources to location

Che et al., 2017

Array Configurations Provide Source Detection and Back Azimuth Estimates

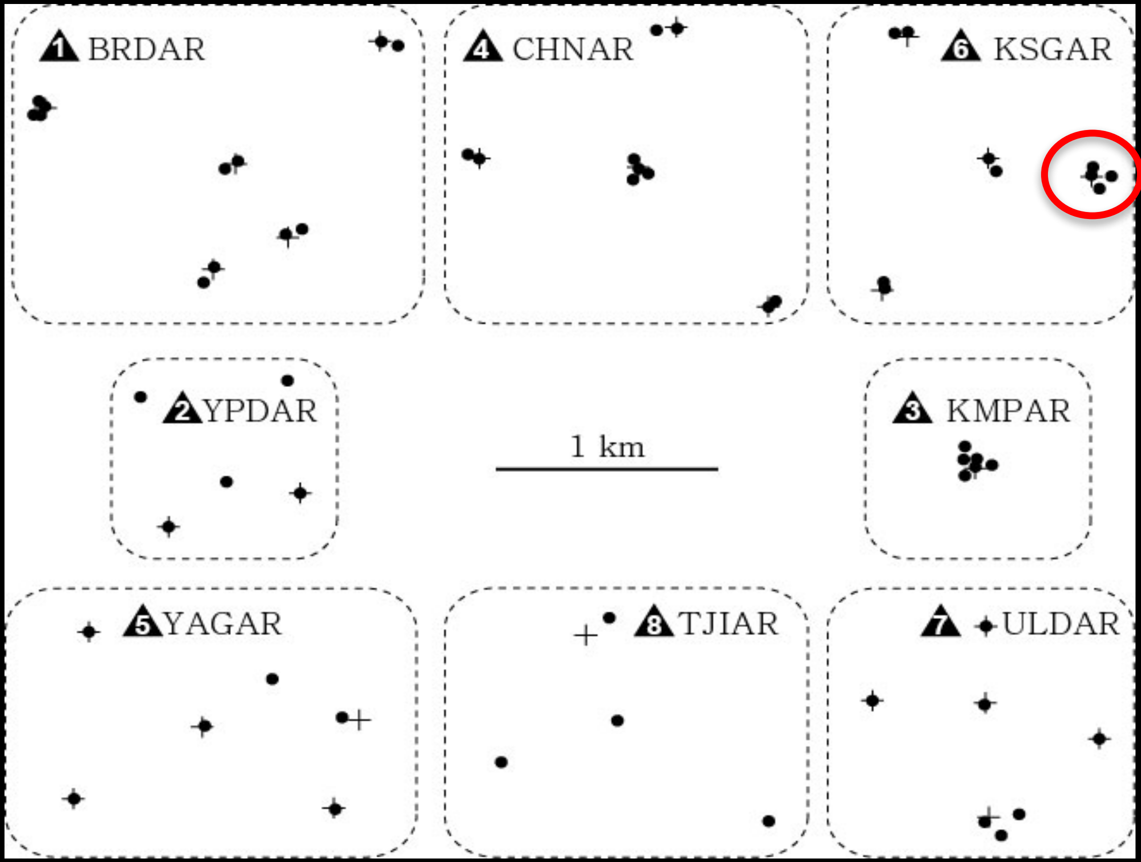

Che et al., 2017

Detection on and around Korean Peninsula of Atmospheric Explosions

- ~10 t of TNT for three-station coverage from June to September
- ~5–30 t of TNT from October to May
- ~20t improvement over IMS stations

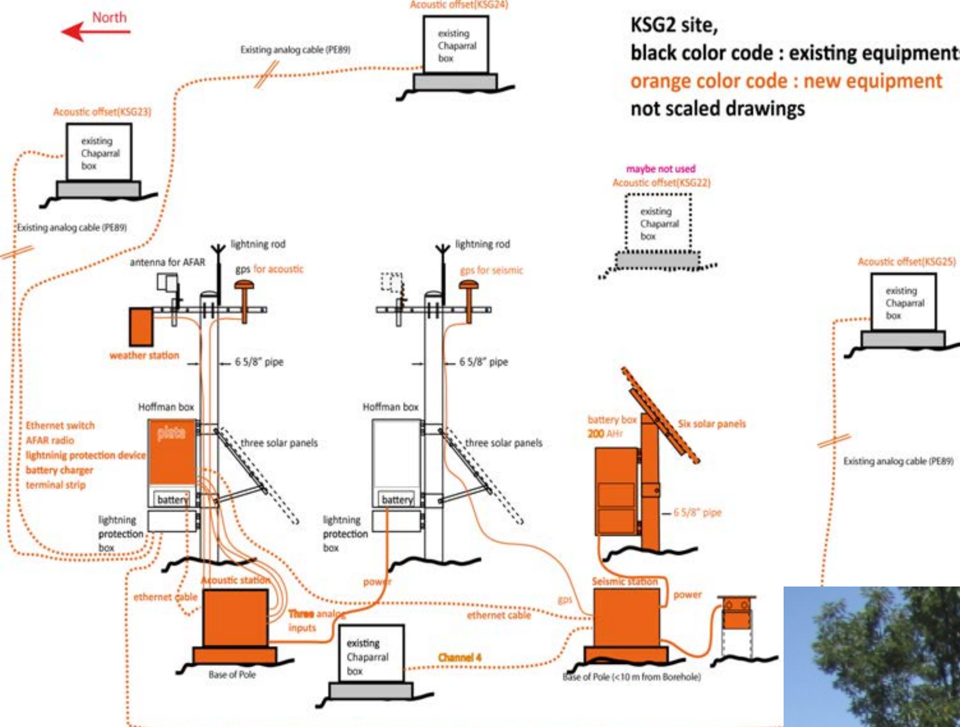

Instrumentation & Arrays

Array Processing *Seismo-Acoustic Event*

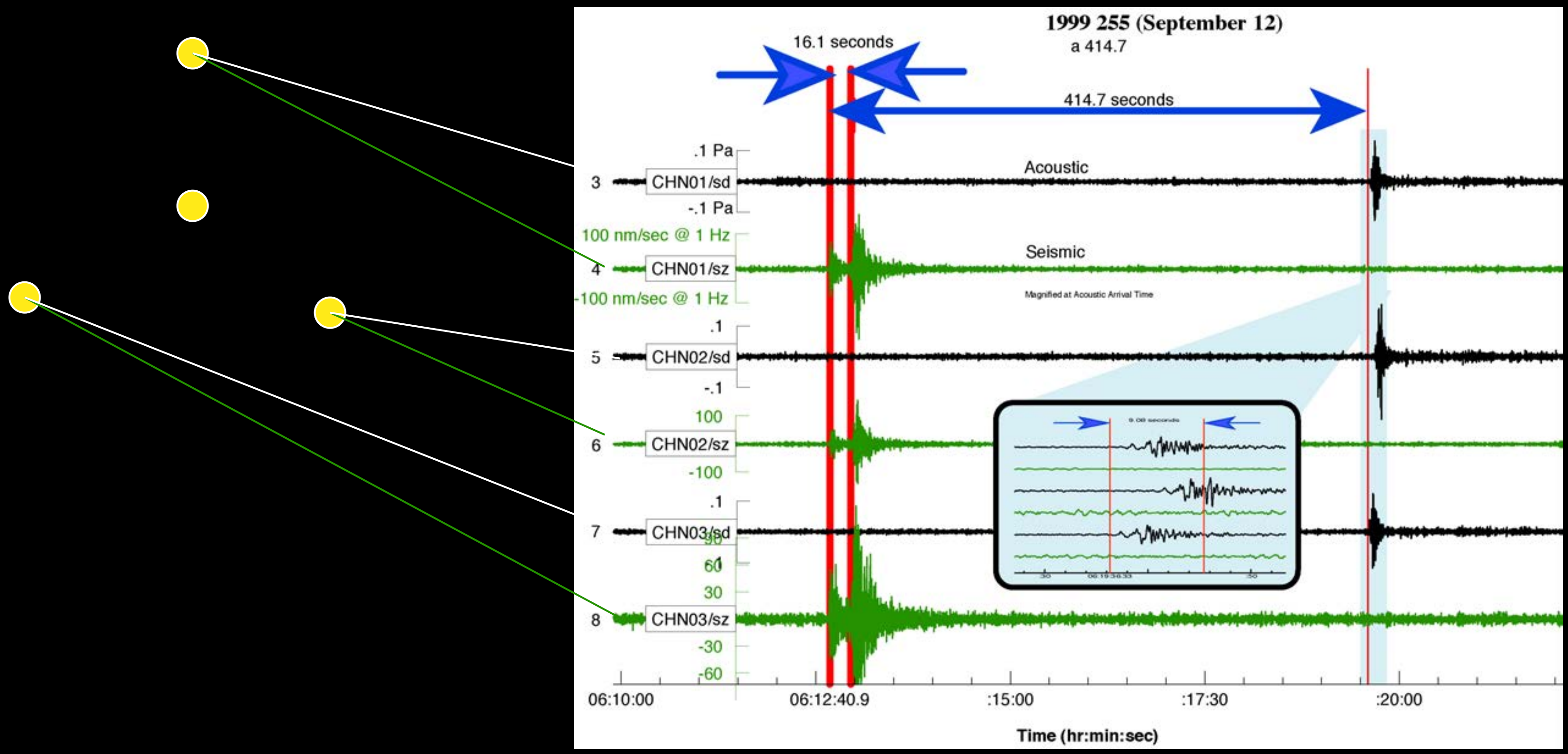

Initially acoustic array processing driven by seismic observation

- Backazimuth
- Phase Velocity
- Phase Identification ?
- Arrival Times ?

Stump et al., 2001

Array Processing and Location

(1) Arrival Time, (2) Backazimuth to Source, (3) Phase Velocity Across Array

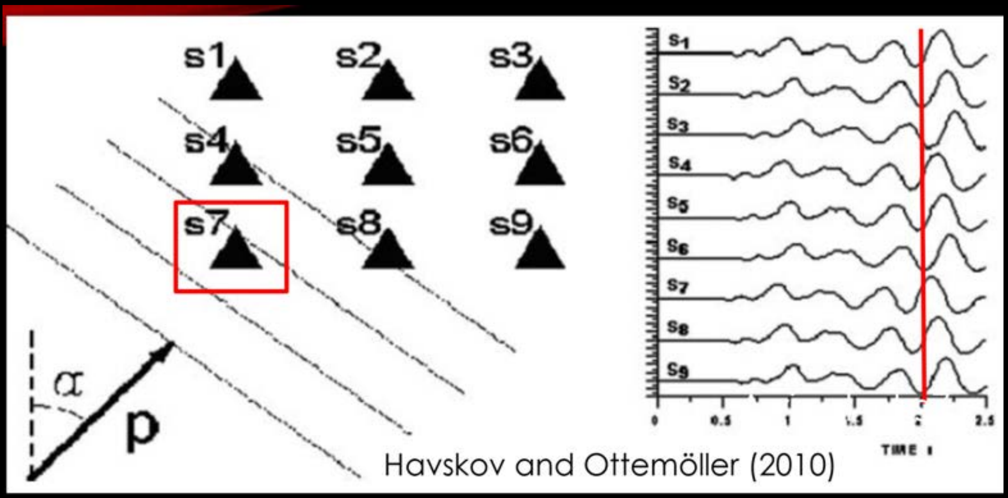

Data and Coherent Data Processing

Rost and Thomas, 2002

Back azimuth model priors

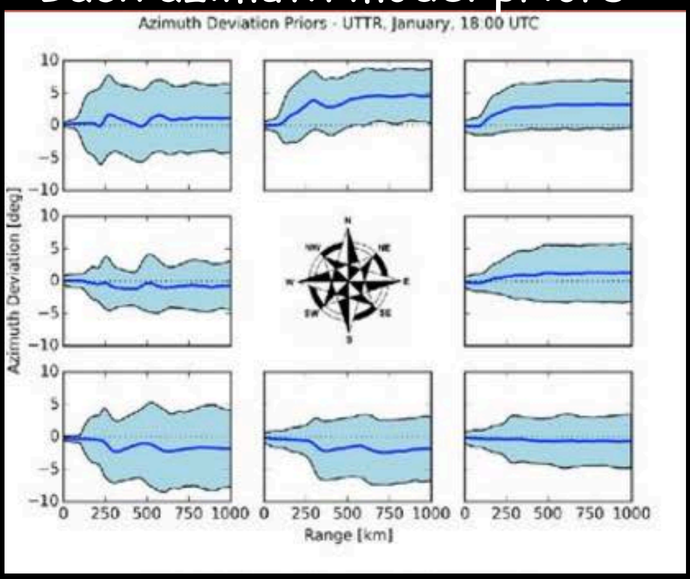

Group velocity model priors

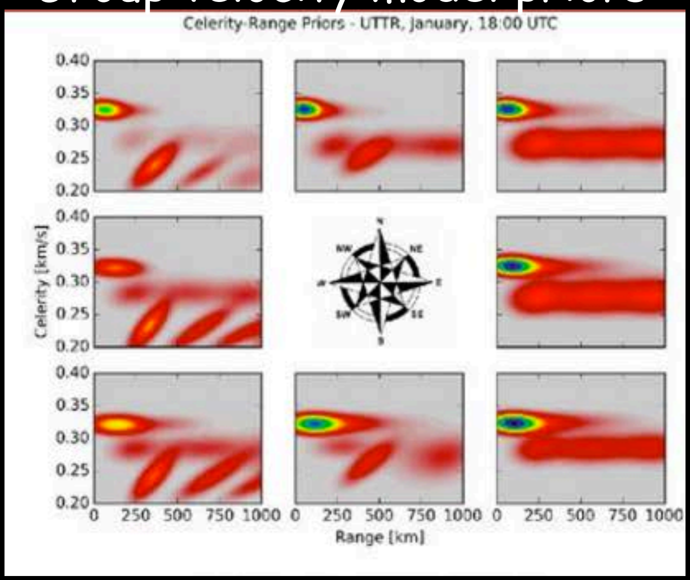

Atmospheric Model

Blom et al., 2015

Infrasound Signals

Detections and Location of Jan 2016 Explosion

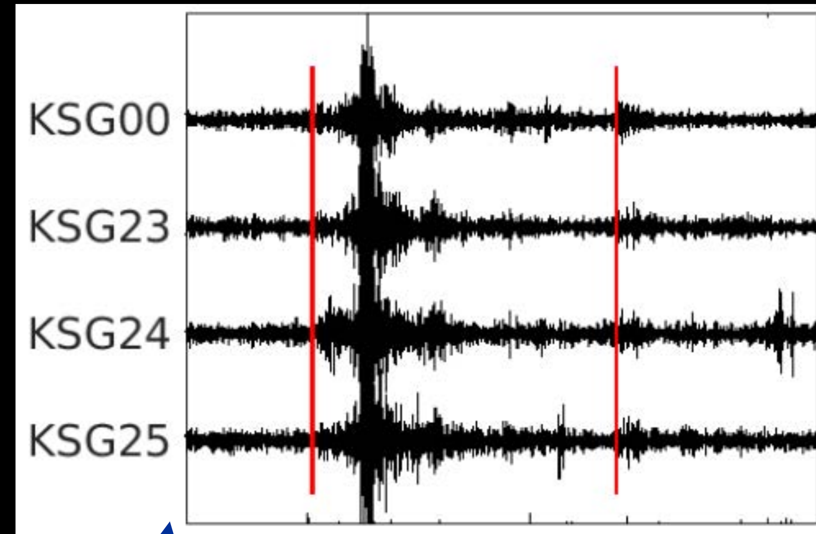

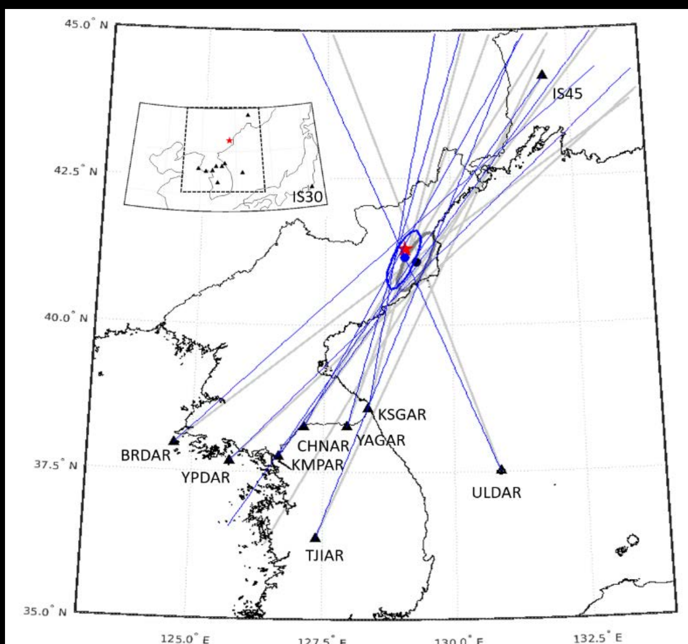

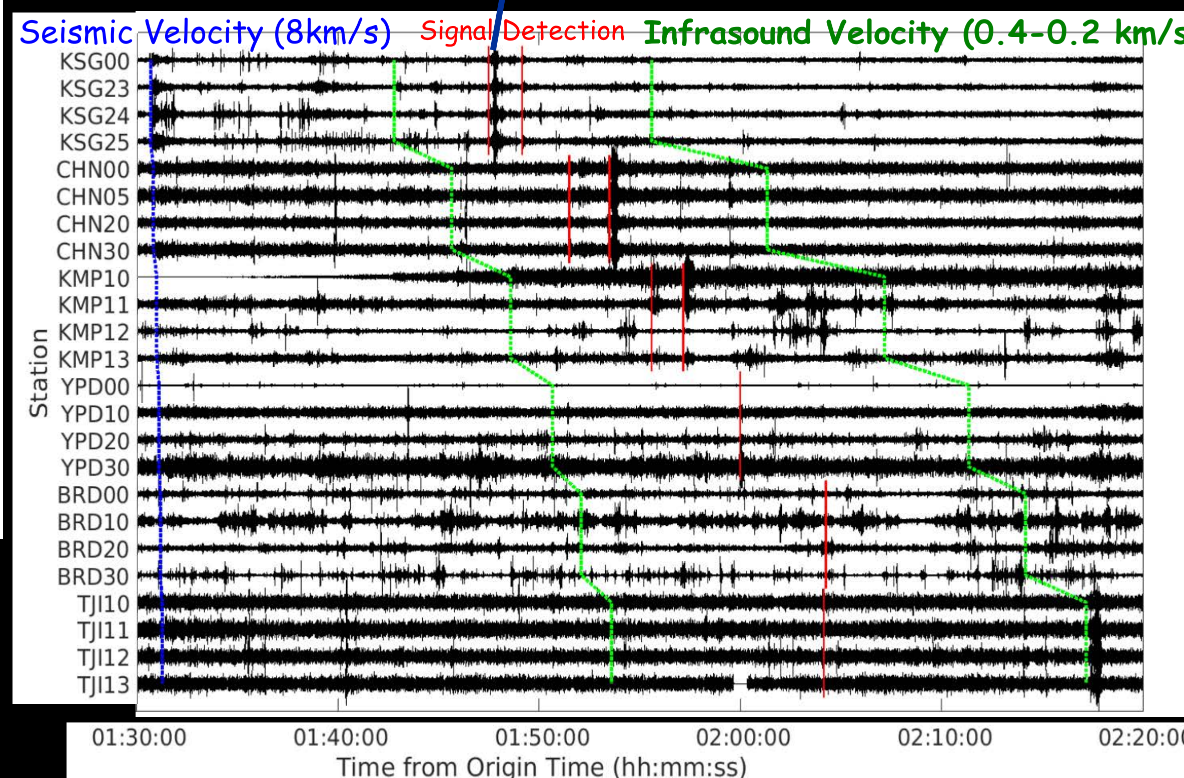

Wind-corrected estimate

Uncorrected estimate

★ Source location

Park et al., 2017

Seismo-Acoustic and Infrasound Sources

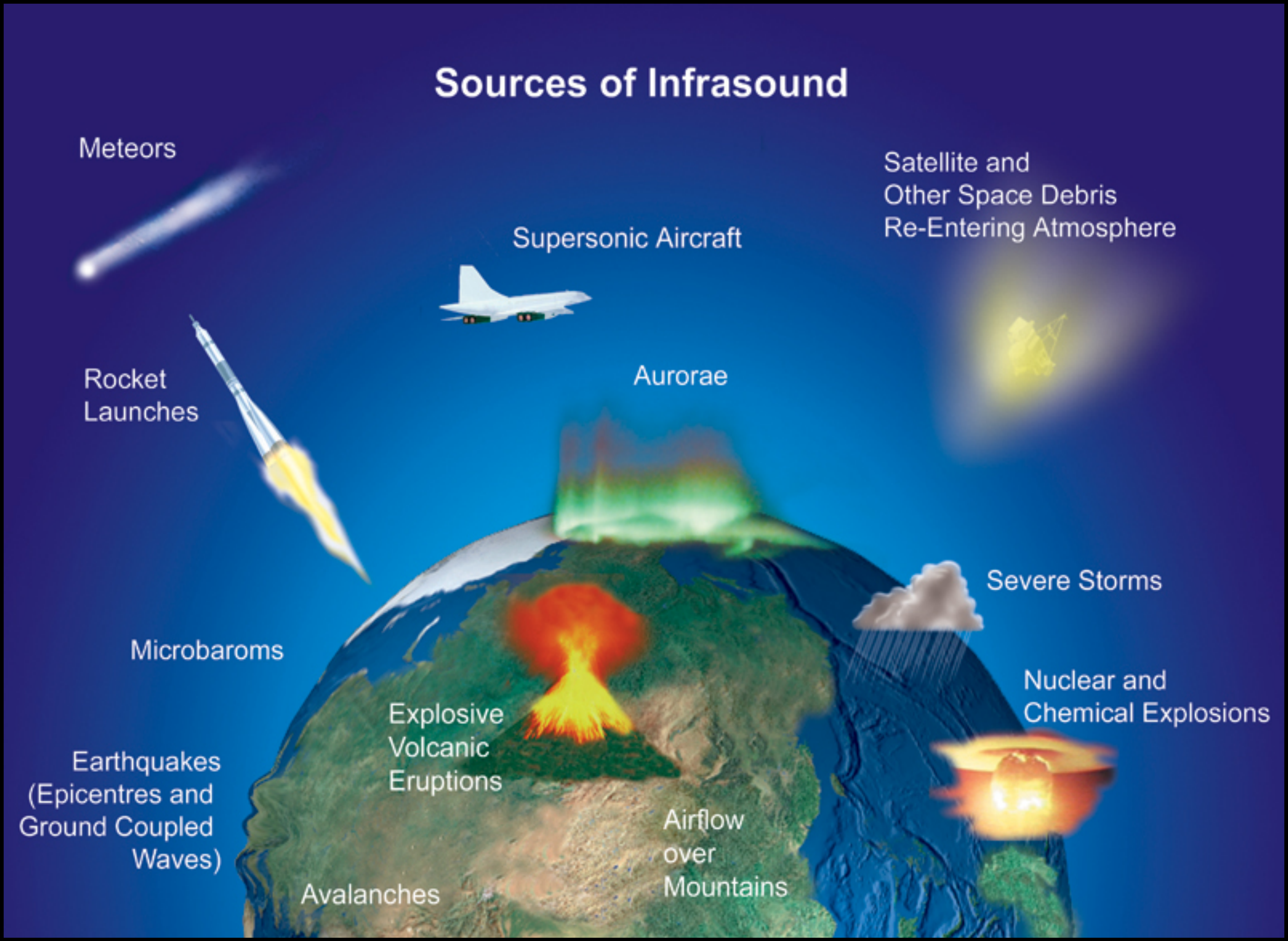

Regional Seismo-Acoustic Signals from Mines

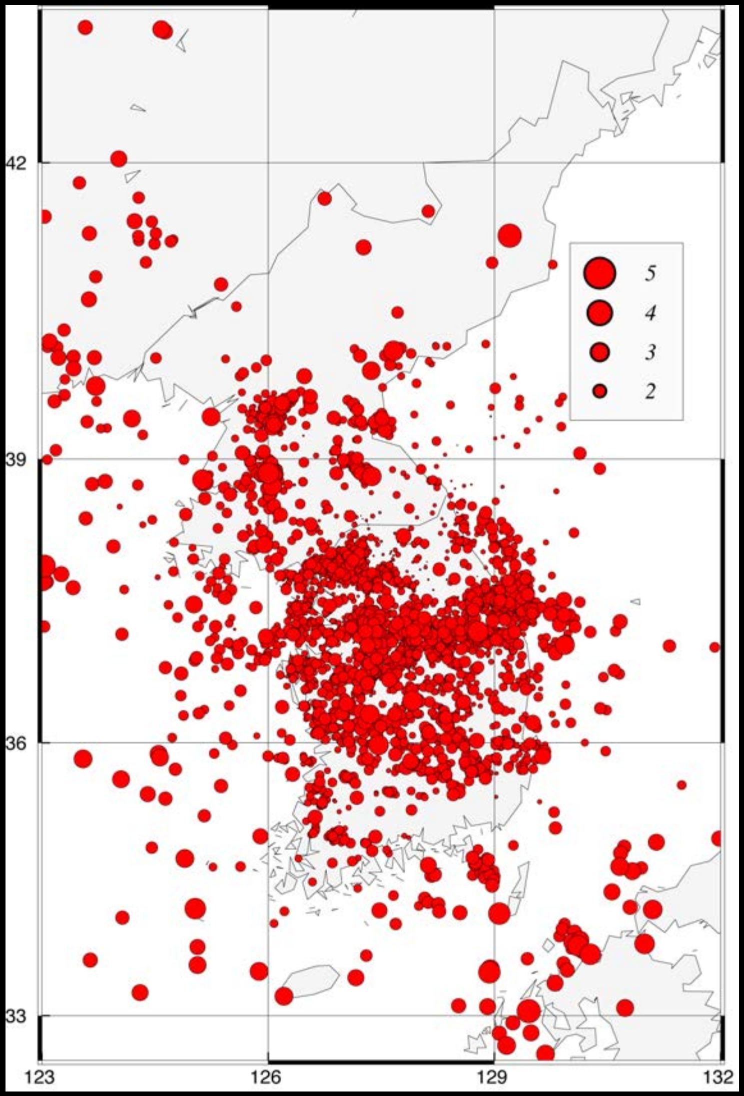

Seismic

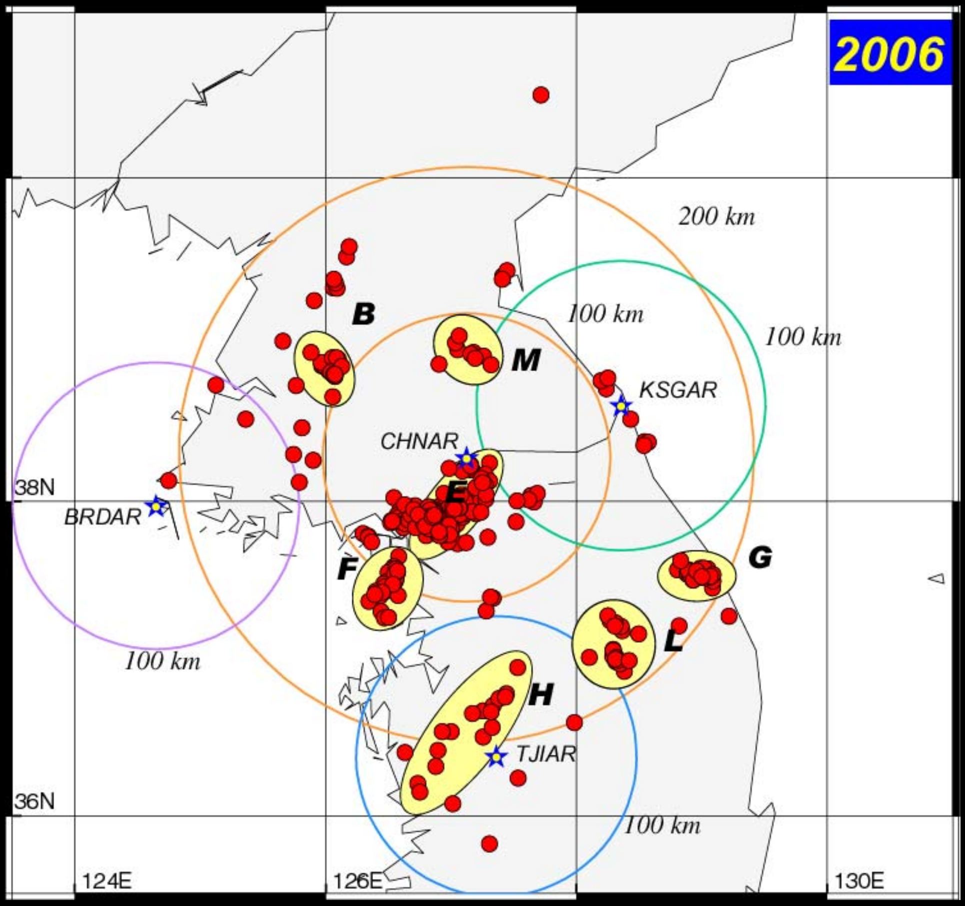

Seismo-Acoustic Signals

Che, 2008

Infrasound Sources

NK Presumed Nuclear Explosions

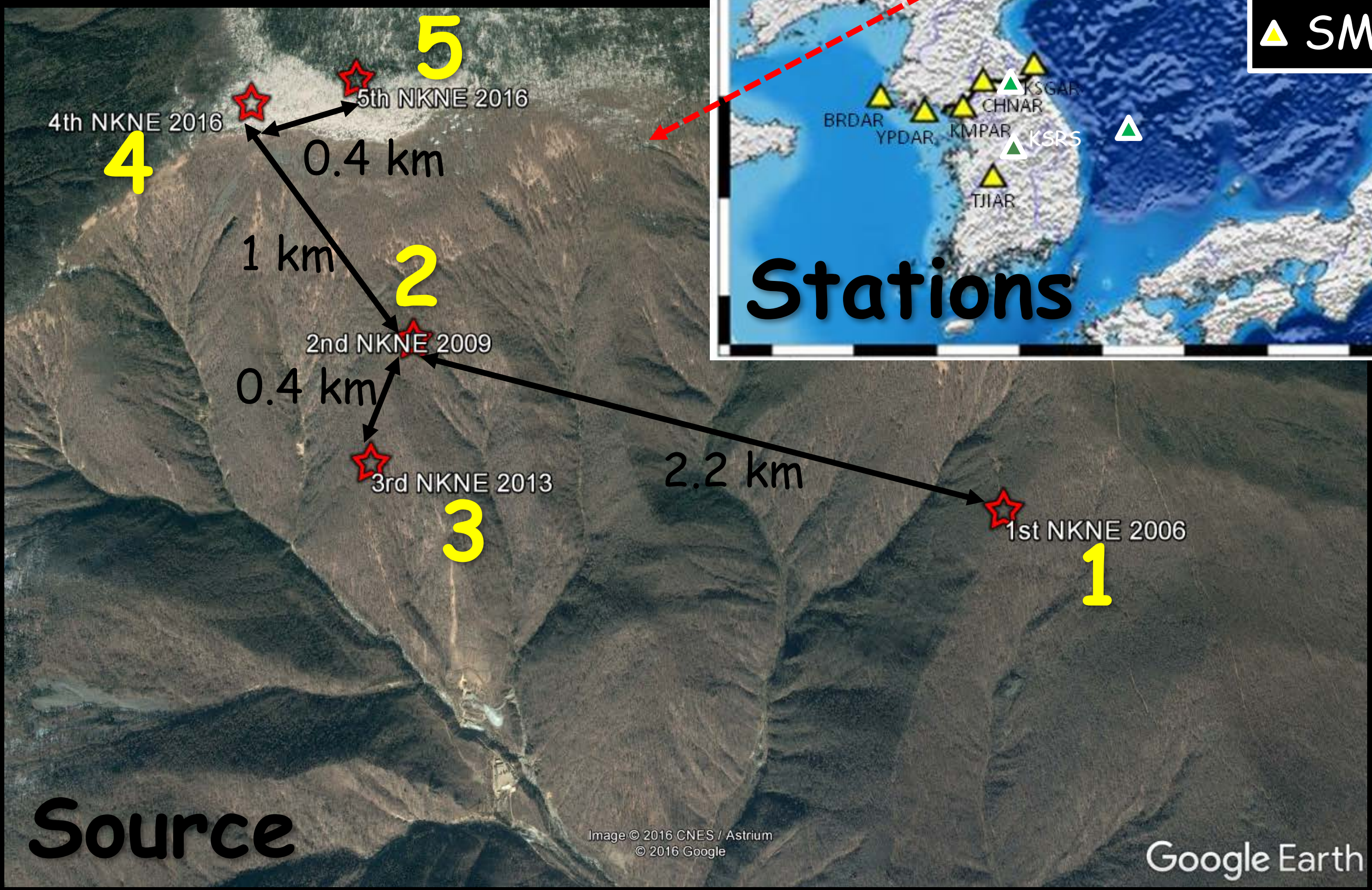

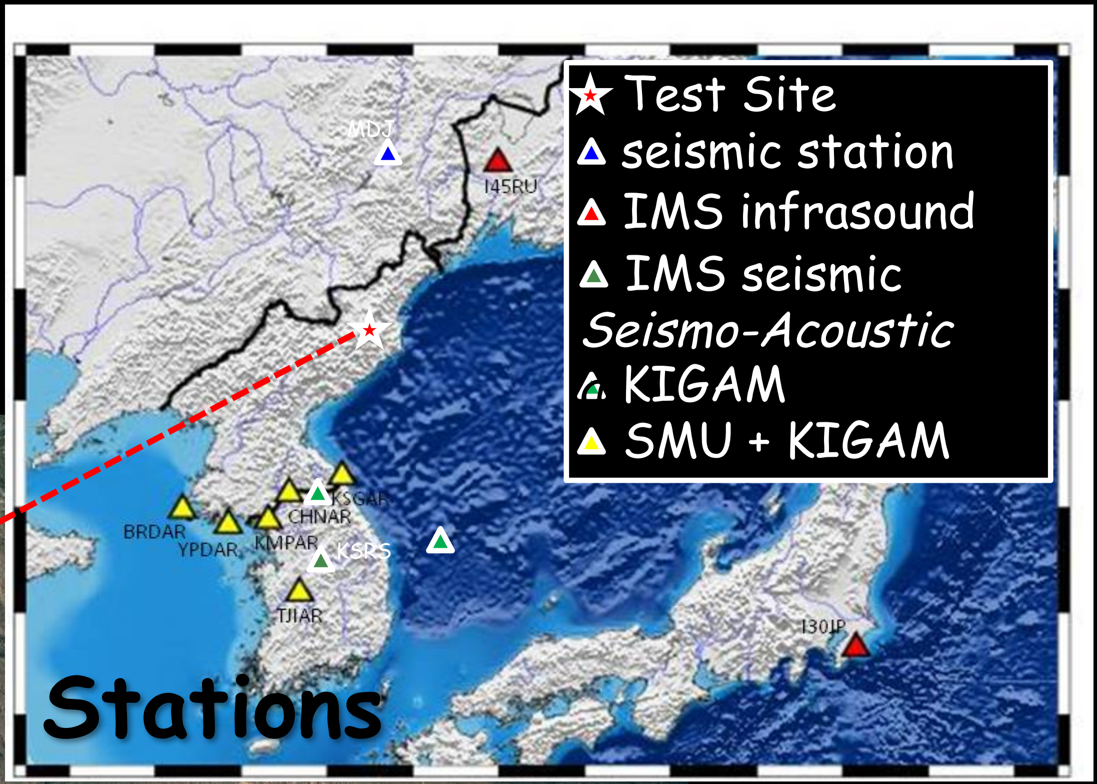

Source location estimates by KIGAM

NK Nuclear Explosions
Infrasound – 2006, 2009, 2013

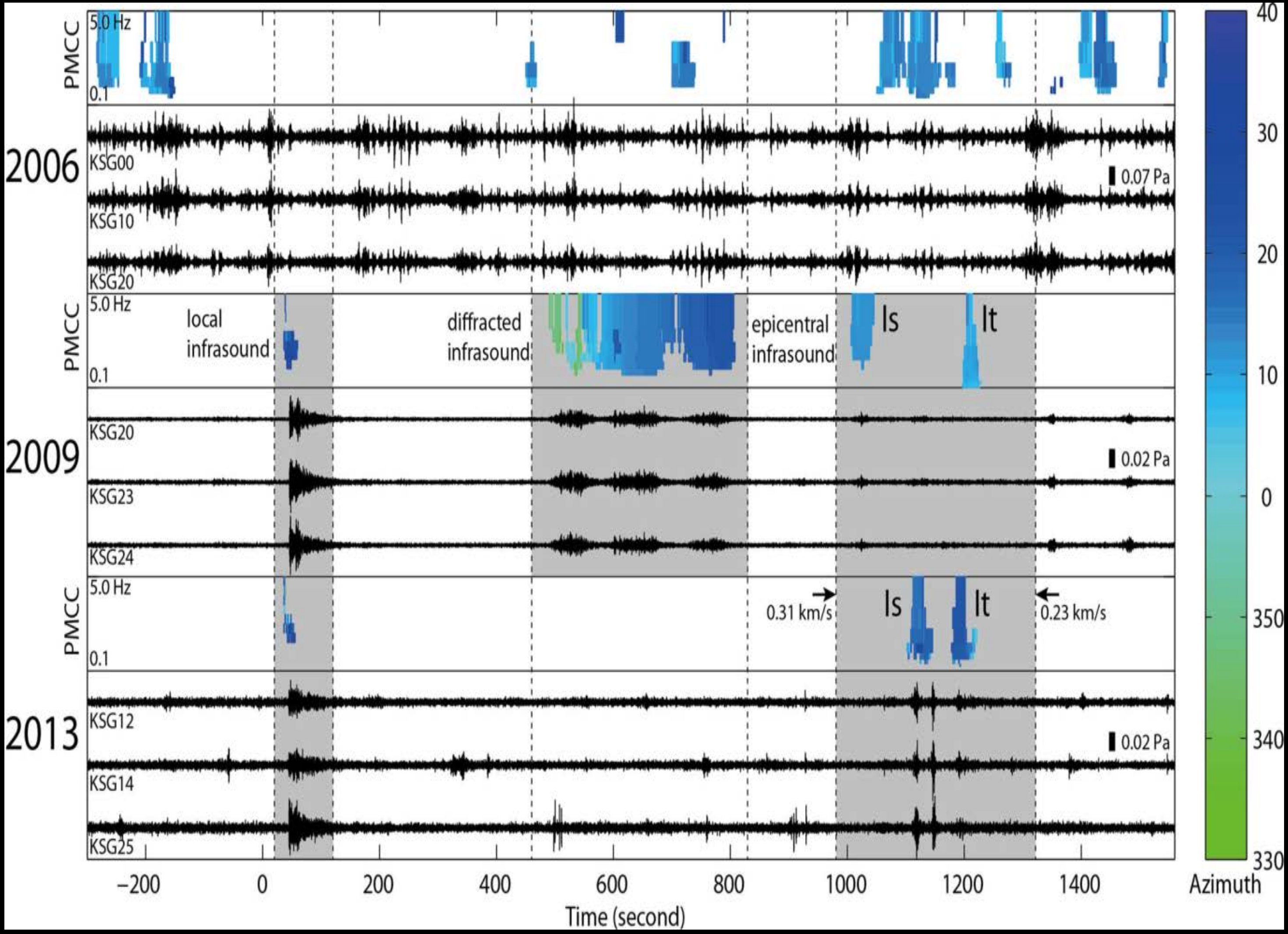

Che et al., 2017

Infrasound Signals

Detections and Location of Jan 2016 Explosion

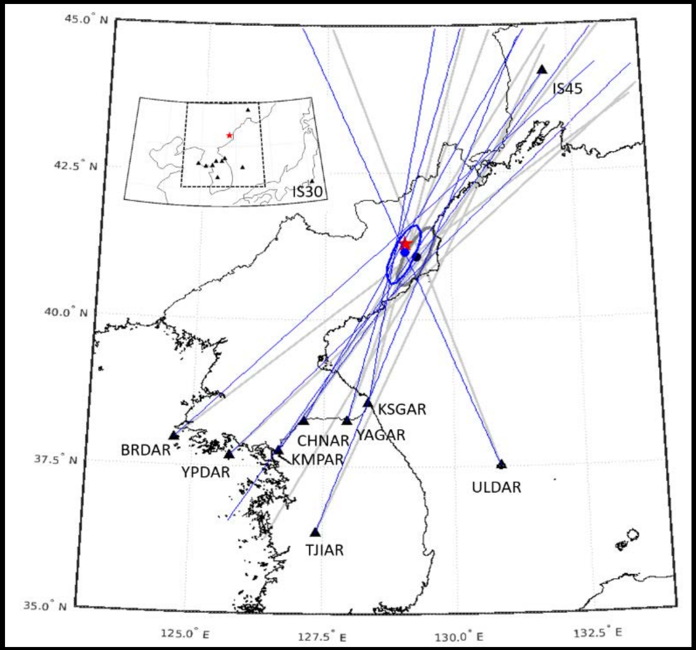

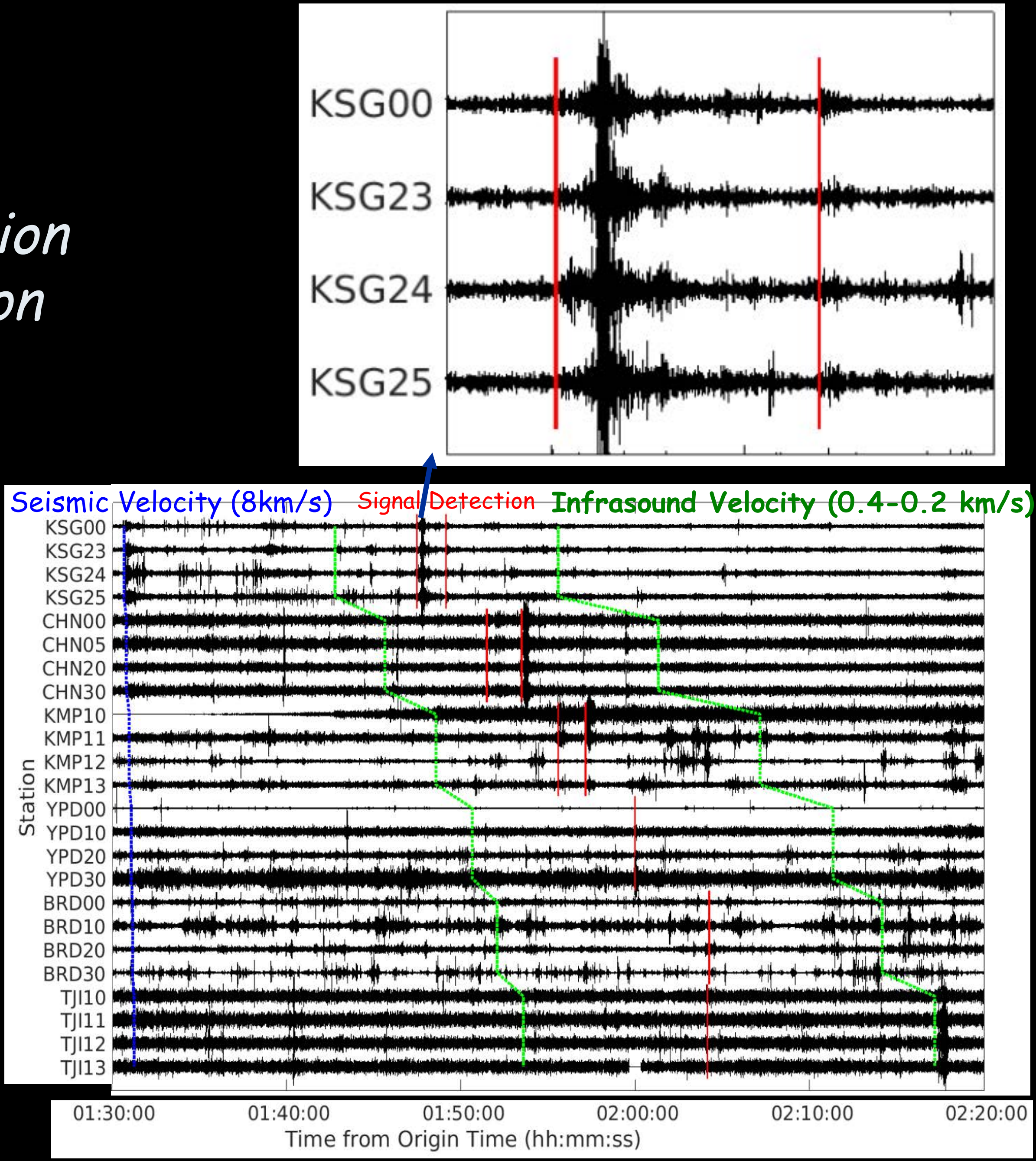

Wind-corrected estimate

Uncorrected estimate

★ Source location

Park et al., 2017

Atmospheric Variations

Predictions - Atmospheric Variations

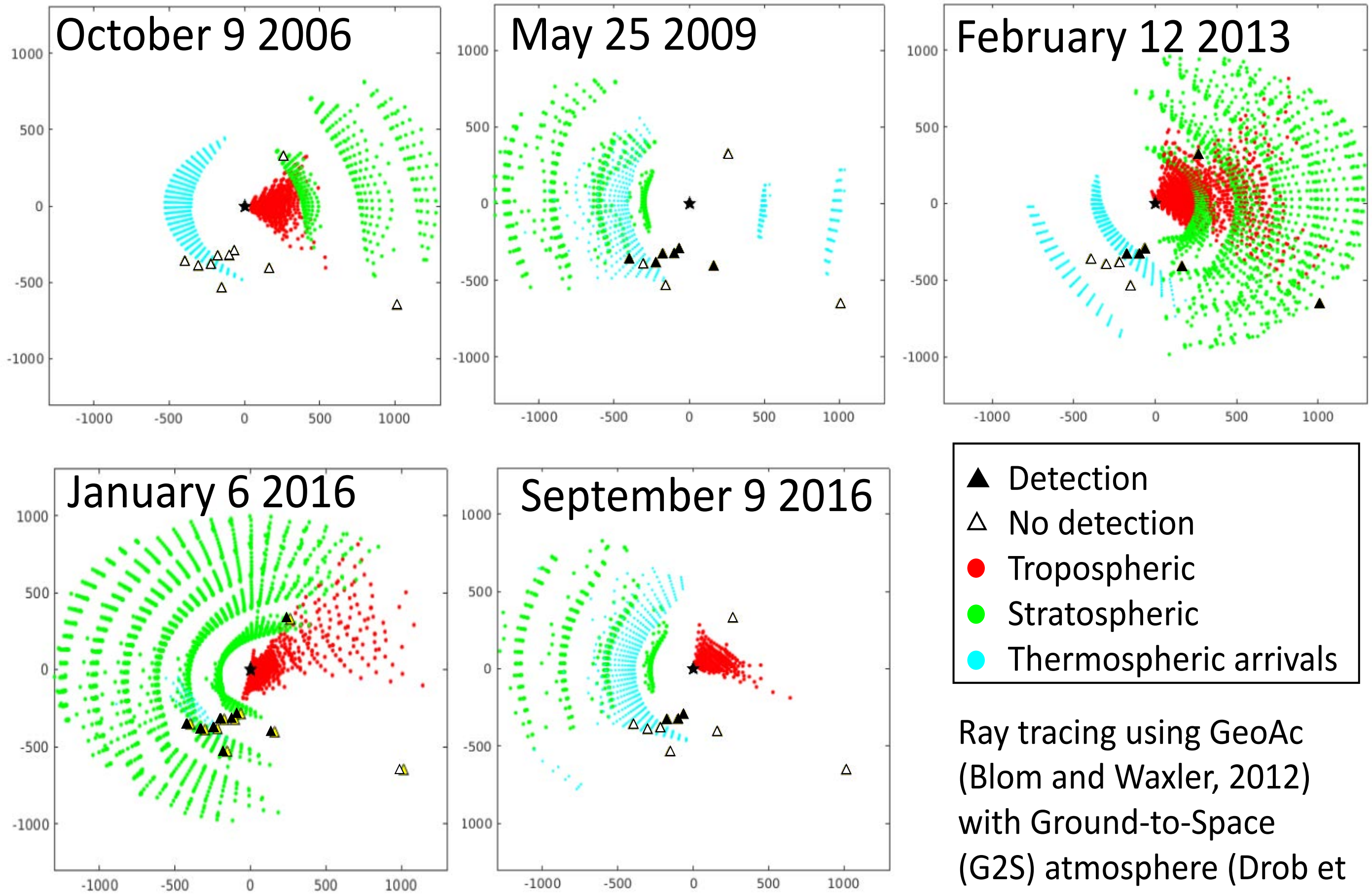

Ray tracing using GeoAc (Blom and Waxler, 2012) with Ground-to-Space (G2S) atmosphere (Drob et al., 2010).

Infrasonic Source Energy

- Empirical yield-scaling from Whitaker et al. (2003)
- Stratospheric phase at closest array (KSGAR)
- Stratospheric wind correction from G2S model
- Equivalent yields:

NKNE	mb	Date	*Tons of TNT*
1st	3.9	10/09/06	-
2nd	4.5	05/25/09	0.6
3rd	4.9	02/12/13	23.5
4th	4.8	01/06/16	8.2
5th	5.0	09/09/16	-

- No clear observations from 2006 explosion and no stratospheric phase at KSGAR for 2016 (Sep) explosion.

Park et al., 2017

Circleville, Utah Earthquake
M_L 4.6, h ~ 9 km

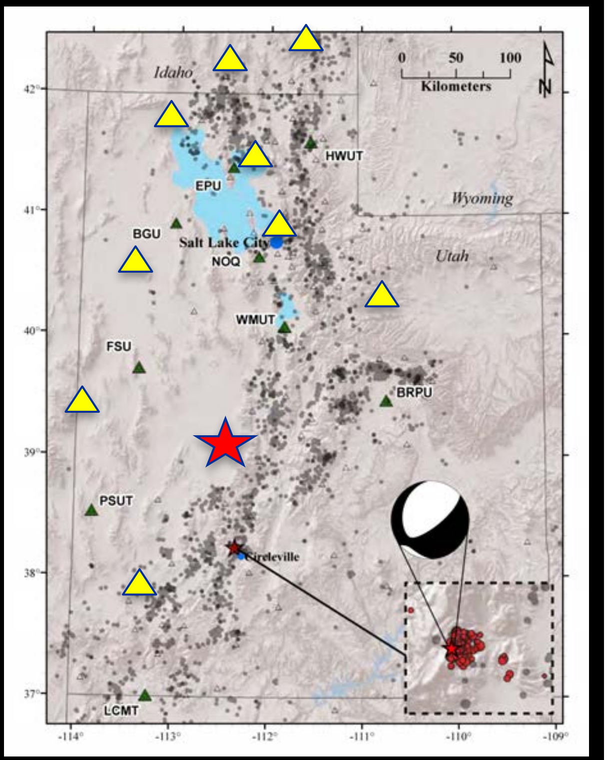

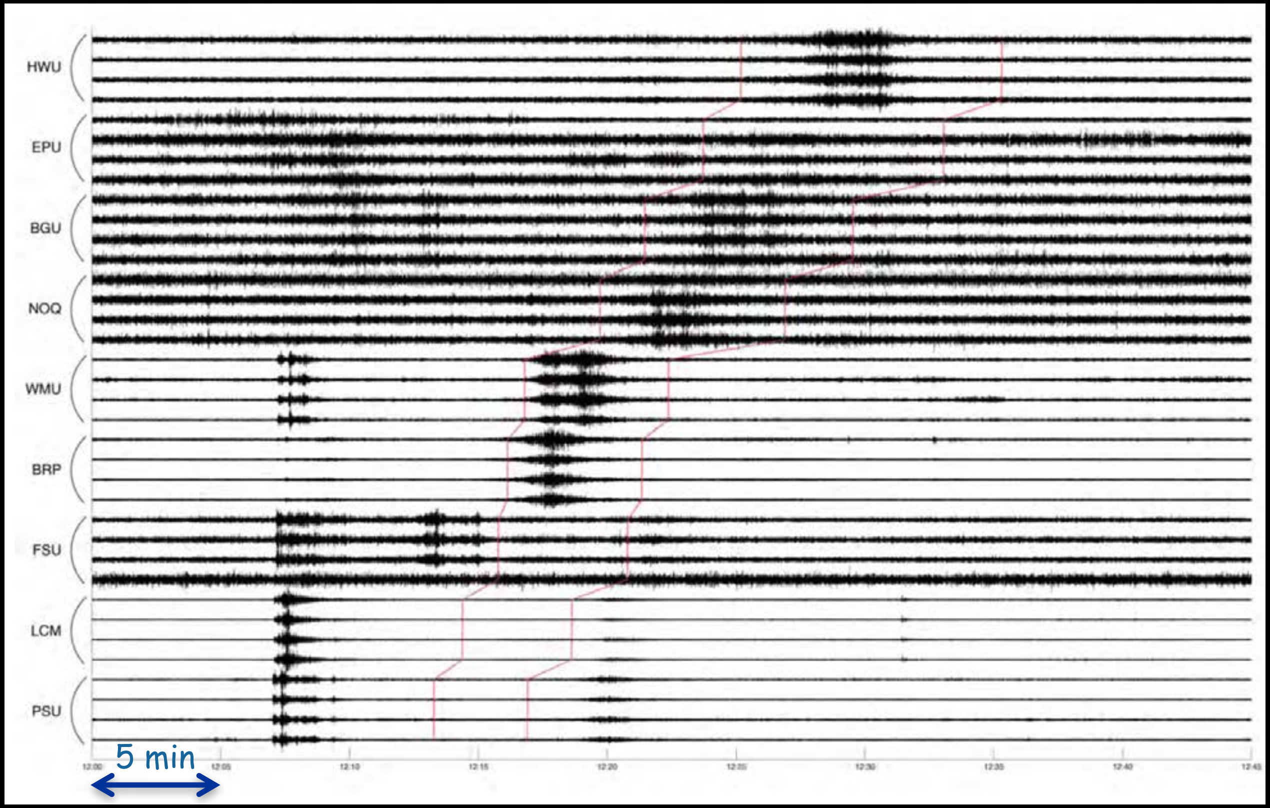

Infrasound observations across arrays deployed in Utah

Arrowsmith et al., 2012

Infrasound Signals and Earthquake Source Location

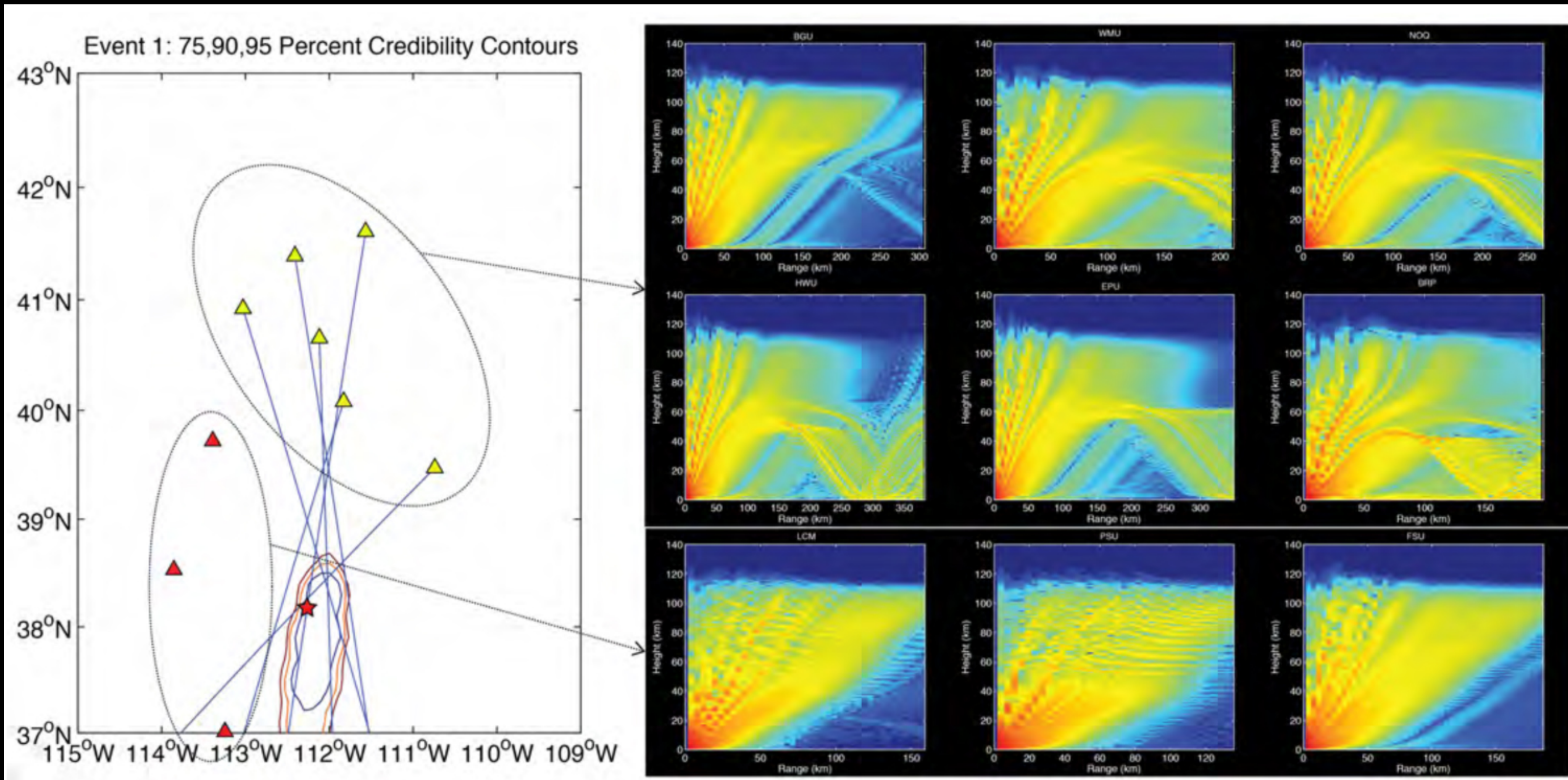

BISL Location

PE Synthetics ~ 1 Hz, Stations with and without observations consistent with synthetics using the G2S atmospheric model

Arrowsmith et al., 2012

Modeling Earthquake Infrasound

Following Pierce (1989) the Rayleigh integral can be used to estimate the near field infrasound given the acceleration time history at the free surface, a(t)

$$p(R_0,t) = \frac{\rho}{2\pi}\int \frac{a(r,(t-R/c))}{R}\,dA_s$$

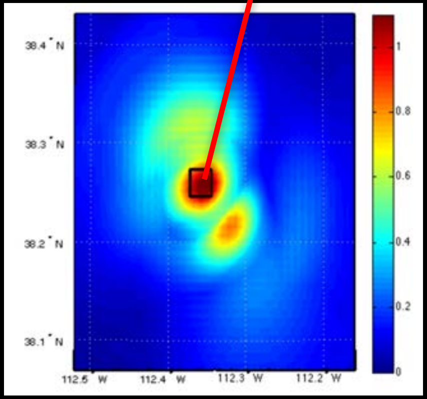

3D Synthetics are scaled by ShakeMap Amplitudes

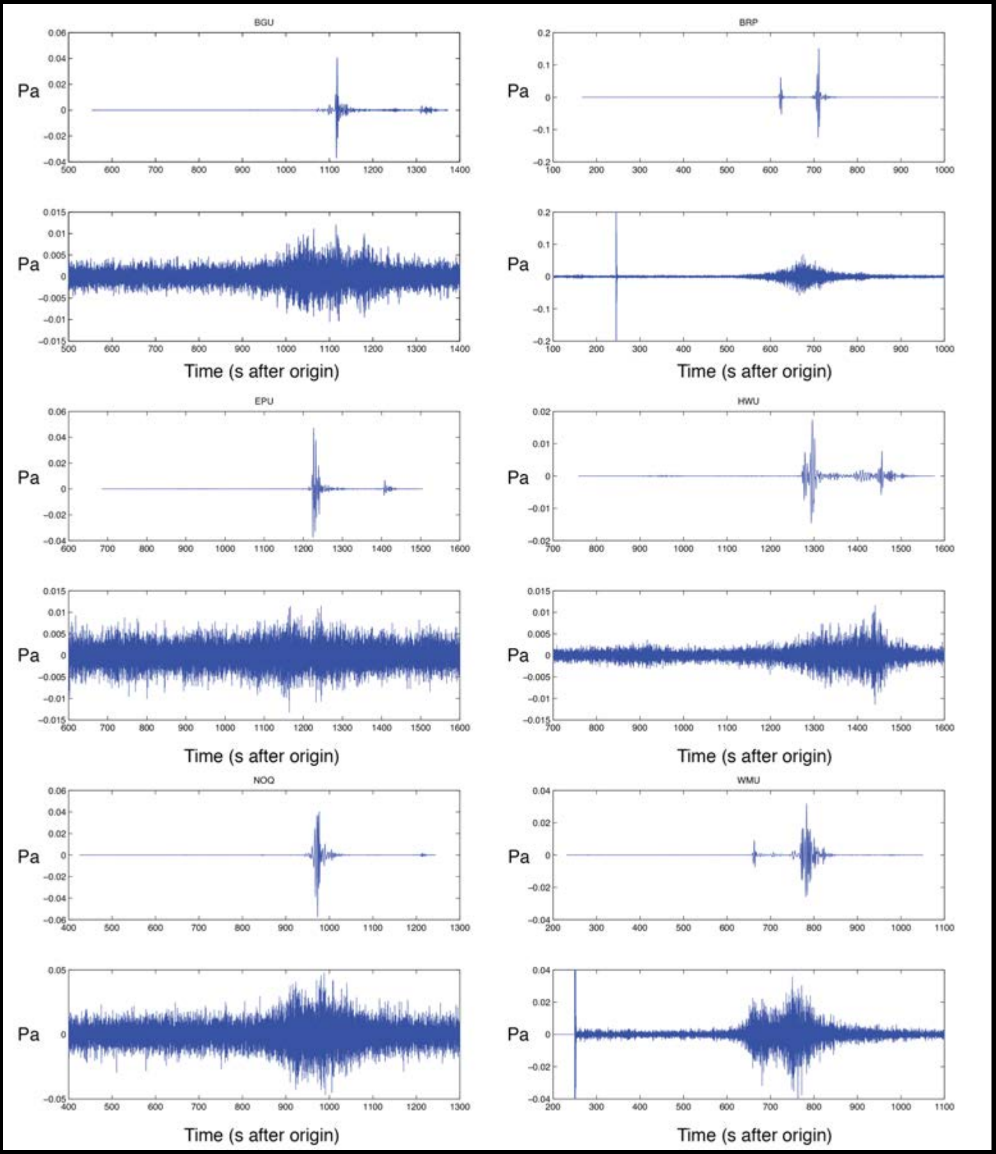

Predicted and observed amplitudes ~ factor 2

Arrowsmith et al., 2012

Infrasound From Volcanoes

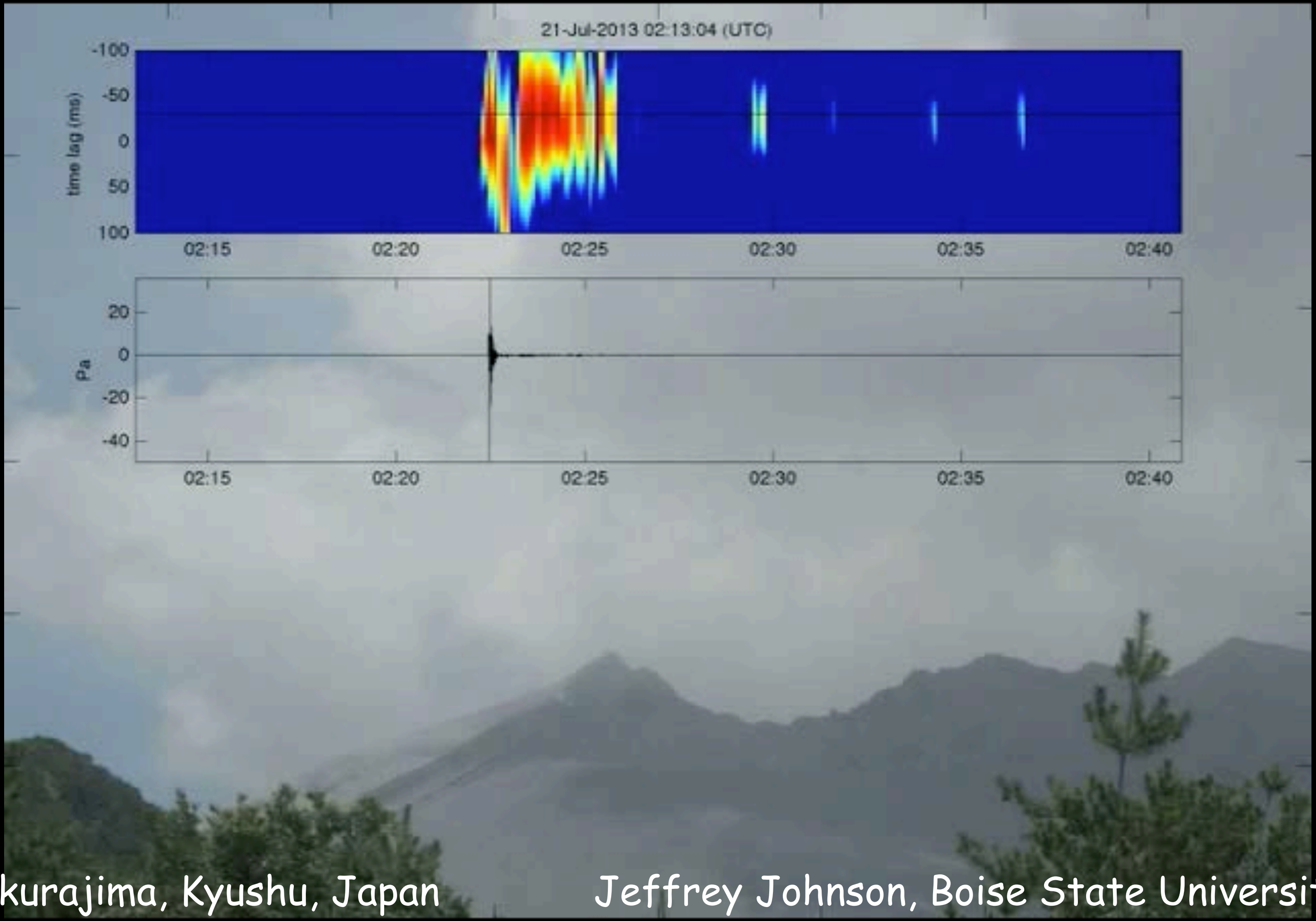

Sakurajima, Kyushu, Japan

Jeffrey Johnson, Boise State University

Bolides

Chelybinsk, 15 Feb 2013

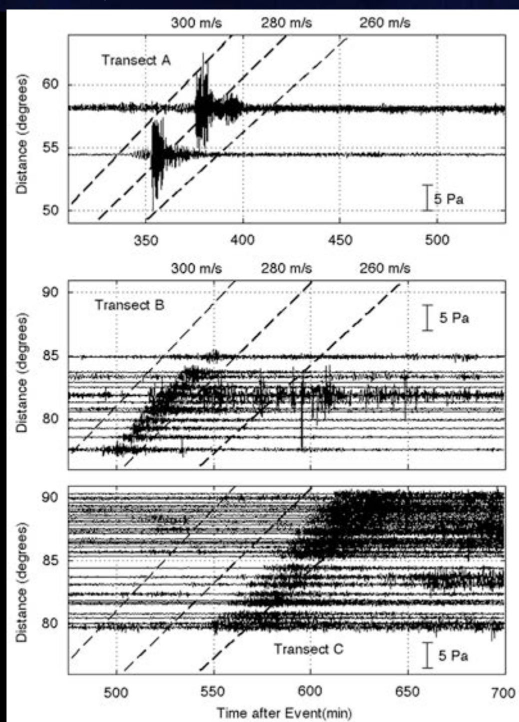

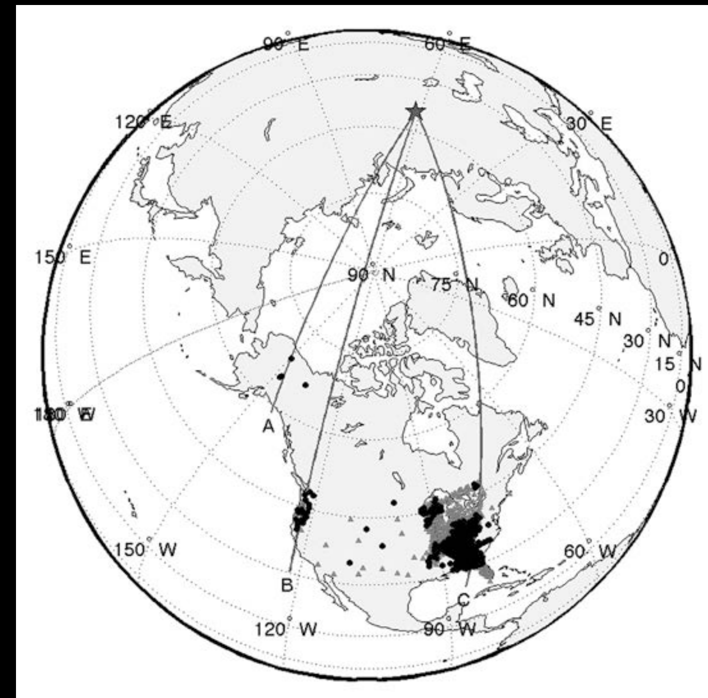

USArray Observations

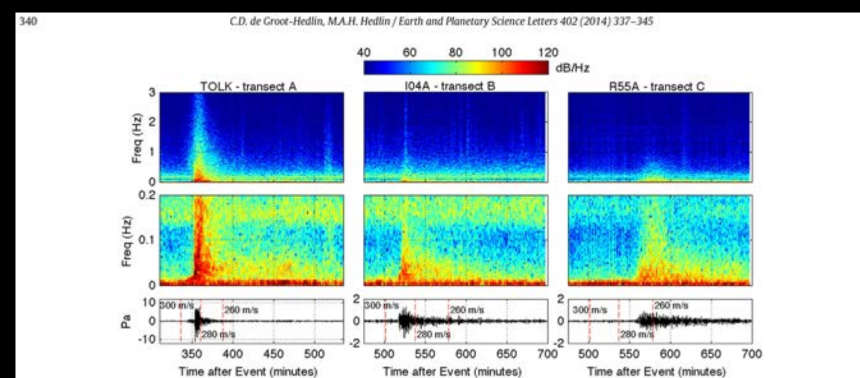

Fig. 3. Spectrograms and bandpassed waveforms for (left column) Alaska station TOLK at [68.6° N, 149.6° W] along transect A at a distance of 54.4° from the source (middle column) station I04A along transect B at [43.8° N, 122.4° W], 81.3° from the source, and (right column) station R55A along transect C at [38.3° N, 80.2° W], 81.2° from the source. The power spectral densities are in dB with respect to a reference pressure of 20 μPa. Each column shows (top) a spectrogram for frequencies up to 3 Hz; (middle) a detail of that spectrogram up to 0.2 Hz; (bottom) a waveform bandpassed from 0.008 to 0.12 Hz. 225 min of data are shown for each station. Arrival times corresponding to velocities of 300, 280, and 260 m/s are marked on each waveform. Note the change of scale of the band-passed waveforms for transect A vs. transects B and C.

Infrasound Sources

De Groot Hedlin and Hedlin, 2014

Forensic Use of Infrasound and Seismic Signals

On 12 August 2015, the city of Tianjin in Northern China was rocked by a series of explosions. The explosions occurred in a facility that housed hazardous chemicals.

Data from local stations in China are not available. The explosions, however, were large enough to be recorded at regional stations in China and Korea.

Goal – Perform an analysis (**location, depth, yield**) of the explosions using multi-phenomological observations (**seismic, acoustic, craterology**) using only **regional** data since local data may not be for future events.

Pasyanos et al., 2016

Regional Infrasound

Regional Infrasound Picks

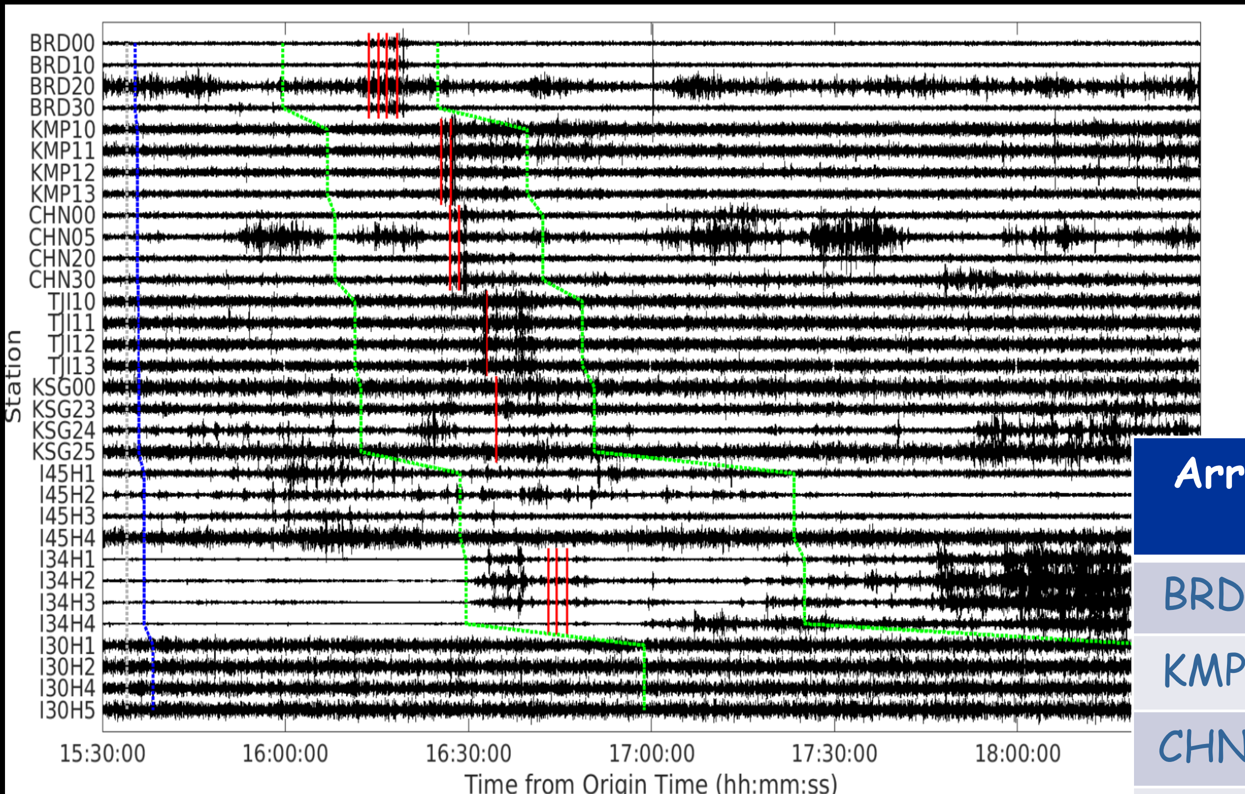

Infrasound waveforms
0.1-2 Hz

Origin Time
Seismic Velocity (8km/s)
Infrasound Velocity (0.4-0.2 km/s)
Signal Detections

Array	Arrival Time	Back Az
BRDAR	16:13:41	280.5°
KMPAR	16:25:31	290.0°
CHNAR	16:27:02	274.6°
TJIAR	16:33:04	295.9°
KSGAR	16:34:37	275.4°
IS34MN	16:46:10	135.9°

Pasyanos et al., 2016

Combined Regional Location

Seismic and acoustic signals are combined through BayesLoc

Infrasound used as a prior for seismic solution

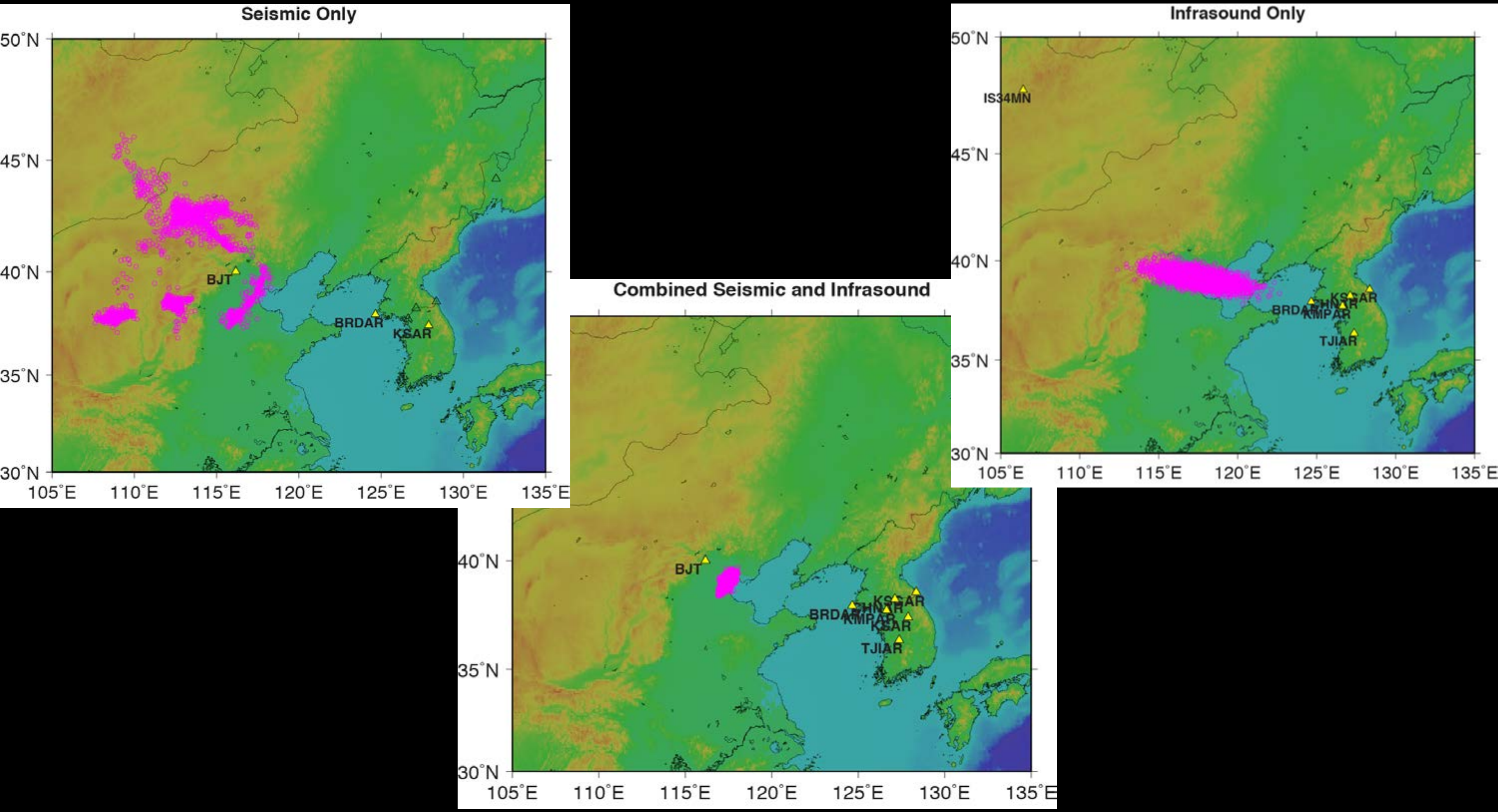

Pasyanos et al., 2016

Combined Yield Results - Hardrock

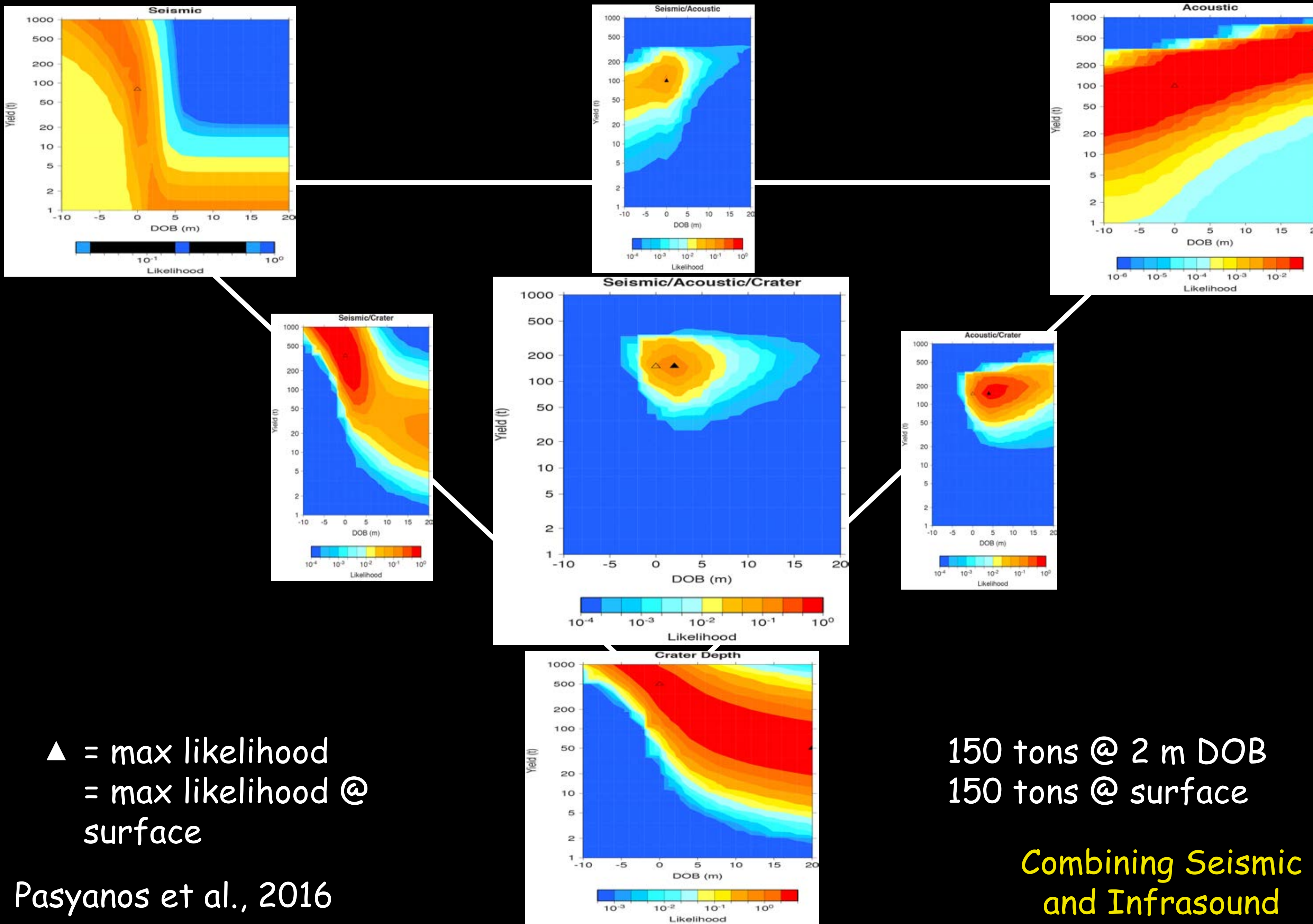

▲ = max likelihood
△ = max likelihood @ surface

150 tons @ 2 m DOB
150 tons @ surface

Pasyanos et al., 2016

Combining Seismic and Infrasound


URBAN INFRASOUND 1
NASCAR Race
10 Seismic Sensors
11 Infrasound Sensors
Seismo-Acoustic Array
1100 Feet
A2
1
2
3
4
5
6
7
8
9
10
11
12
13
14
15
TEXAS
SUNOCO
Greenhills Dr
Country Ln Cir
Lone Star Cir
293 m
© 2014 Google
USGS
Google earth
Imagery Date: 4/10/2013
1995
lat 33.036744° lon -97.278963° elev 194 m
Eye alt 1.47 km
Combining Seismic and Infrasound

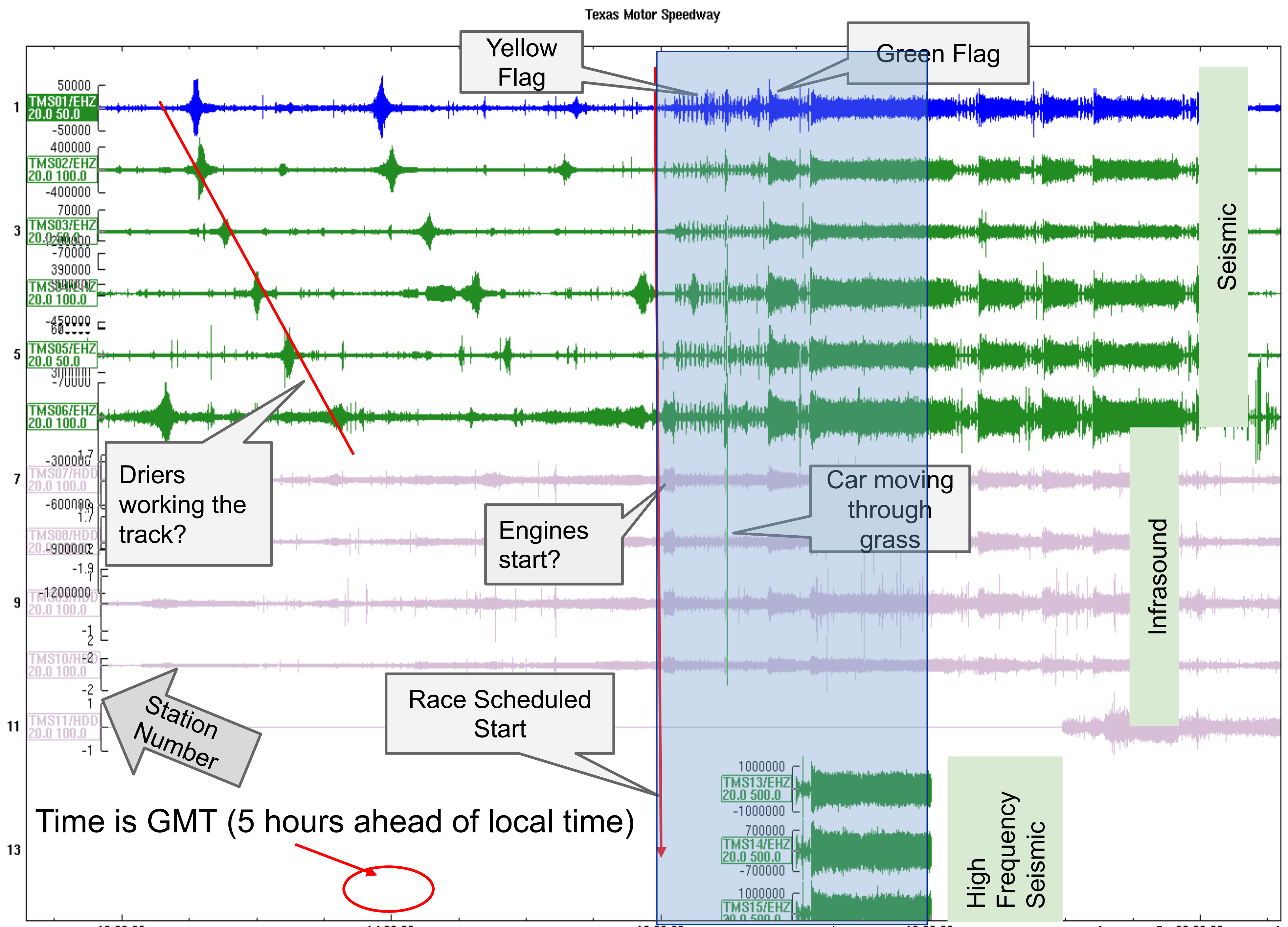

Combining Seismic and Infrasound

Details Just Before and After Race Start

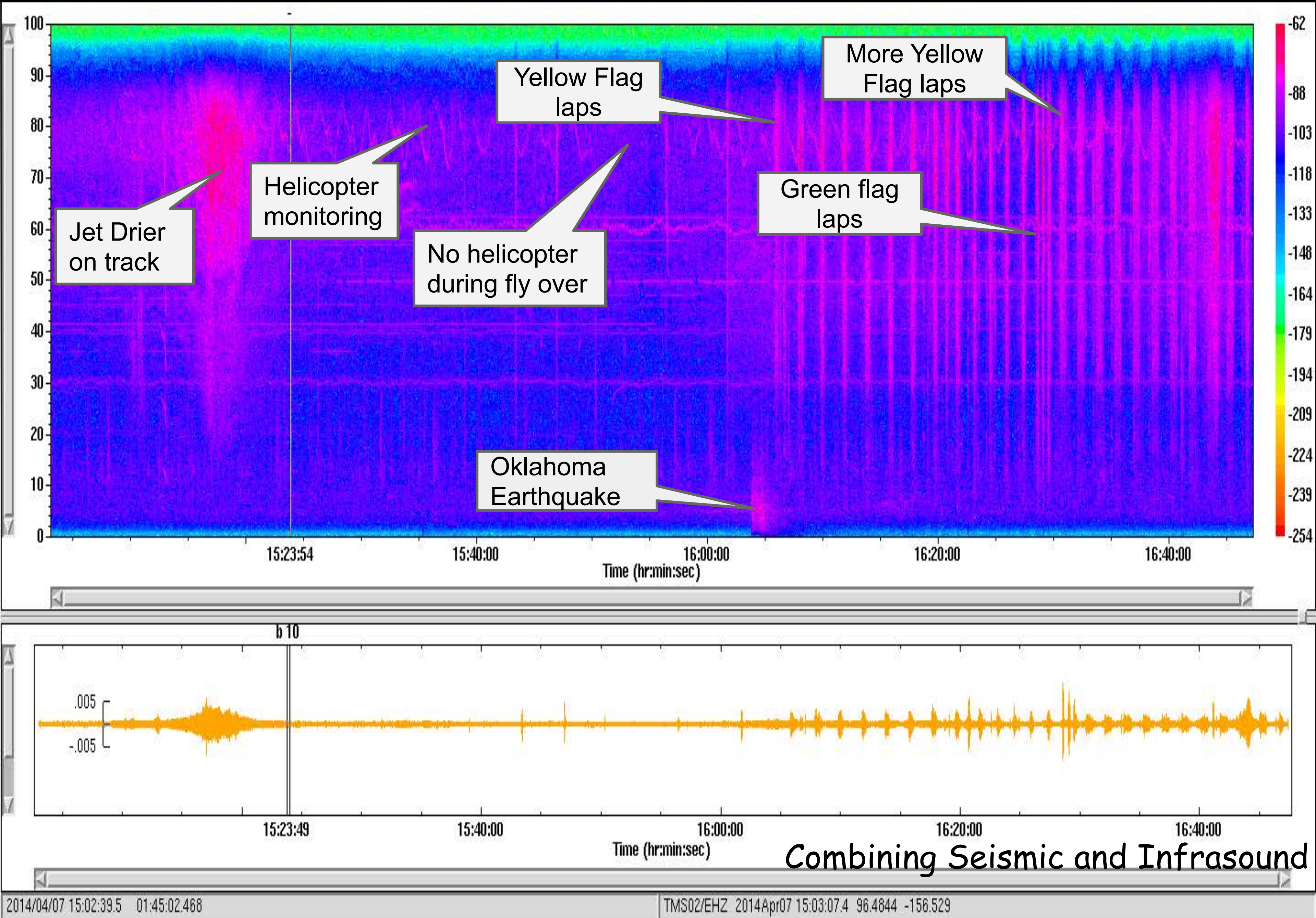

Combining Seismic and Infrasound

Conclusions

- Infrasound signals have been used for over 100 years to ID natural and human sources
- Infrasound wavelengths are a factor of 10 smaller than typical seismic wavelengths.
- Infrasound propagation is time dependent.
- Arrays are critical to separating infrasound signals from noise.
- Many opportunities for combining seismic and infrasound observations.